Probabilistic mapping of earthquake-induced submarine landslide susceptibility in the South-West Iberian margin

Stefano Collico[a,*], Marcos Arroyo[b], Roger Urgeles[c], Eulàlia Gràcia[c], Marcelo Devincenzi[a], Norma Peréz[d]

[a] Igeotest s.l, Figueres, Spain
[b] Department of Civil and Environmental Engineering (DECA), Universidad Politecnica de Cataluña, Barcelona, Spain
[c] Department of Marine Geosciences, Institut de Ciències del Mar (CSIC), Barcelona, Spain.
[d] Department of Environmental Geology and Geohazards, ICTJA, CSIC, Spain

ABSTRACT

The SW Iberian continental margin is well recognized as a tectonically active area, where major canyons and mass wasting events are both present. Earthquake triggered submarine landslides may cause tsunami and result in catastrophic damage to bordering coastal areas. In this setting, submarine landslide susceptibility mapping represents a major step towards a regional risk mitigation strategy. Landslide susceptibility mapping in large offshore areas presents significant challenges as a result of the limited information on controlling variables, large uncertainties in triggering mechanisms and limited geotechnical data. In this study, a geotechnical model-based approach has been followed that narrows the range of controlling factors and, within a probabilistic framework, allows a systematic treatment of parameter uncertainties. This model-based analysis covers the whole SW Iberian margin increasing by three orders of magnitude the areal extent of precedent offshore slope stability susceptibility studies. This jump in spatial scale is facilitated by application of a systematic Bayesian updating procedure, to combine geotechnical information from global databases and that available from regional sites. Seismic shaking is estimated using an available regional database of seismogenic faults. These tools are implemented within a GIS to generate, via Montecarlo simulations, probabilistic landslide susceptibility maps based on two different analytical seismic infinite slope stability models. These models differ mainly in the form of their final results, either as distributions of slope stability safety factors or as distributions of seismic-triggered slope displacements. Receiving Operator Curves are used to assess the different landslide susceptibility predictions obtained against a comprehensive regional database of submarine landslides. It turns out that the models analyzed correctly predict 92% and 82% of the mapped landslide subset chosen for validation for pseudo-static and displacement-based method respectively. This suggests that, within the limits of the currently available databases, seismic events are the dominant factor at the origin of the submarine landslides mapped in the study area. An advantage of the framework presented is that it can quickly incorporate new regional geotechnical information or better regional landslide databases, as they become available.

1. Introduction

Submarine landslides are widespread in all continental margins and compared to their subaerial counterparts, they have larger magnitude and frequently occur on gentler slopes (Hühnerbach et al., 2004; Chaytor et al., 2009; Urgeles and Camerlenghi, 2013; Behrmann et al., 2014; Huhn et al., 2019). Submarine landslides may impact directly on underwater structures and are also capable of generating destructive tsunami waves (Synolakis et al., 2002; Løvholt et al., 2019). Several historical and instrumental examples prove the connection between earthquakes and submarine landslides (e.g., Piper et al., 1999; Geist, 2000; Sassa and Takagawa, 2018) and earthquakes are generally recognized as the main triggering mechanism for tsunami-generating offshore landslides (ten Brink et al., 2009; Grilli et al., 2009).

Incorporation of landslide generated tsunamis into probabilistic tsunami hazard assessments is considered particularly difficult (Grezio et al., 2017), as large uncertainties affect the probability and location of slope failures. Susceptibility maps are used to predict where a landslide
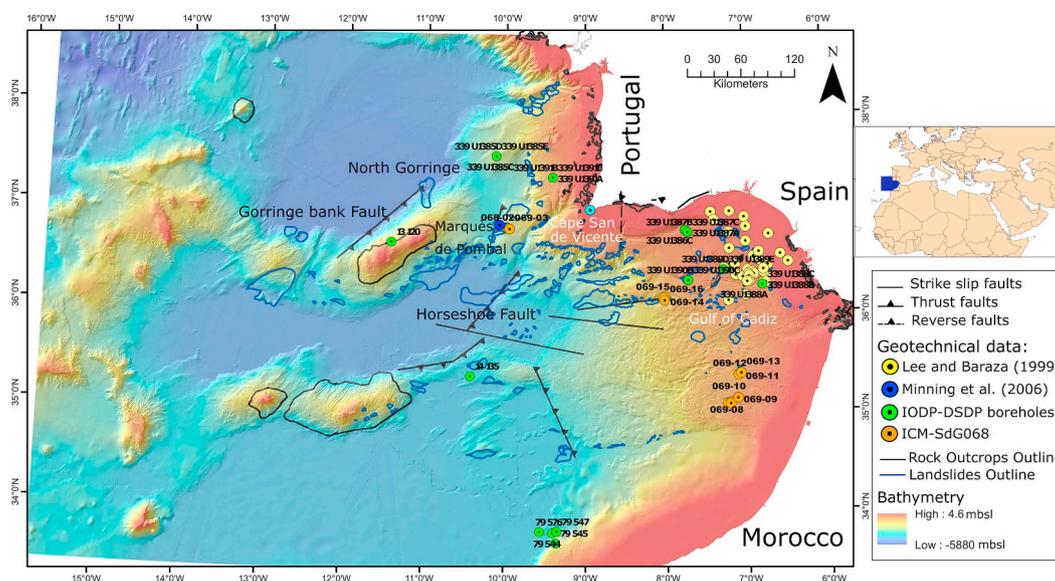
Fig. 1. Study area with bathymetric information (EMODnet Bathymetry Consortium, 2018), location of sites with geotechnical data (Table 1), surface trace of faults (Basili et al., 2013) and catalogued landslide areas.

is likely to occur (Guzzetti et al., 2006) and are recognized as a key step in onshore landslide hazard analyses (Corominas et al., 2014). The intensity of seismic shaking is an important component for landslide susceptibility maps, both onshore (Jibson et al., 2000; van Westen et al., 2008) and offshore (Lee et al., 1999; Urgeles et al., 2002).

There are different approaches to map landslide susceptibility (Reichenbach et al., 2018), including heuristic (or index-based), statistical and probabilistic methods. Heuristic or index-based methods have been applied to map susceptibility offshore (Hitchcock et al., 2010; Leon and Somoza, 2011). However, they express landslide susceptibility in qualitative terms. Statistical methods are used onshore to map landslide susceptibility at regional scales, quantifying the probability of failure (Zhu and Huang, 2006; Chauhan et al., 2010). The application of similar methods offshore (Borrell et al., 2016; Piedade et al., 2018) faces severe difficulties, because the number of thematic variables available for prediction is limited by the scarcer data available.

Quantitative probabilistic prediction is also possible using a process-based approach to map susceptibility (Jibson et al., 2000; Reichenbach et al., 2018). In this approach models are used to represent the physical process producing landslides. For earthquake triggered submarine landslides suitable models may be based on the infinite slope concept with effective stress-normalized undrained strength parameters (Lee and Edwards, 1986).

Lee et al., (1999) integrated a simplified infinite slope models with GIS technology to map spatial variability of slope failure susceptibility in a relatively small area (approx. 400 km^2) offshore California; Urgeles et al., (2002) produced a landslide susceptibility map for the Saguenay Fjord (140 km^2 in Quebec, Canada); Mackenzie et al. (2010) used GIS-based landslide hazard analysis in offshore oil and gas projects with development areas of over 1,000 km^2; Strasser et al. (2011) presented a landslide susceptibility map for the whole of Lake Lucerne (114 km^2). In all these examples the slope stability models were treated deterministically, using best estimates and/or worst-case scenarios, as relevant. Nevertheless, it is desirable to move form deterministic to probabilistic susceptibility assessments, as they offer a more consistent framework to express the effect of inevitable input uncertainties in the results. Probabilistic assessment is also consistent with the needs of tsunami hazard studies (Pampell-Manis et al., 2016; Grezio et al., 2017). Precedent probabilistic approaches using infinite slope models include Carlton et al. (2017) and Puzrin et al. (2017) who mapped landslide hazards for areas not larger than a few hundred km² in the Lofoten

Islands and Caspian Sea respectively. Puzrin et al. (2017) used a more complex model incorporating the concept of shear band propagation in the analysis.

The challenge addressed here is to extend that previous work to the much larger areas involved in regional mapping. For this purpose, the *SW* Iberian margin has the advantage of counting with relatively good databases of both potential earthquake sources and observed submarine landslides. On the other hand, the geotechnical information currently available for the region is rather sparse, as is often the case in most marine studies. This limitation is addressed here, for the first time in mapping landslide susceptibility in the offshore environment, using a Bayesian methodology to combine the existing regional information and that given by worldwide-sourced databases. Bayesian methods are useful because they allow a systematic treatment of uncertainties and they can easily incorporate newly obtained information. These advantages are now widely recognized, both in the field of geotechnical characterization (Wang et al., 2016) and in that of tsunami hazard studies (Grezio et al., 2017).

2. Geological setting

The *SW* Iberian continental margin is characterized by the interplay of complex tectonic activity between the Iberian and African plates. Seismicity is characterized by shallow to deep earthquakes of low to moderate magnitude ($M_w < 5.5$) (Buforn et al., 1995, 2004; Stich et al., 2005; Stich et al., 2007; Stich et al., 2010), but also includes the largest and most destructive earthquakes in Western Europe (1531 CE, 1722, 1755 and 1969) (Fukao, 1973). The 1755 Lisbon Earthquake (estimated $M_w > 8.5$) destroyed the city (intensity X-XI MSK) and was accompanied by tsunamis that devastated the SW Iberian and NW African coasts (Baptista et al., 1998; Baptista and Miranda, 2009). Wide angle seismic data shows that most seismicity is due to onset of subduction west of the Gulf of Cadiz Imbricated wedge (Martínez-Loriente et al., 2014). Active fault structures there correspond to NE-SW trending west-verging folds and thrust faults (Gràcia et al., 2003; Zitellini et al., 2004; Terrinha et al., 2009). In addition, long WNW-ESE dextral strike-slip faults are also present (Zitellini et al., 2009; Terrinha et al., 2009; Bartolome et al., 2012; Hensen et al., 2015).

Submarine landslides are also ubiquitous in Gulf of Cadiz (Urgeles and Camerlenghi, 2013). Infrequent large volume events are capable of tsunami generation (Lo Iacono et al., 2012). In the Gulf of Cadiz (Fig. 1), landslides and turbidites have been used as a proxy for off-fault

paleoseismic seismology. For instance, landslides such as the Marques de Pombal slide and the North Gorringe debris avalanche (Vizcaino et al.,2006; Lo Iacono et al., 2012), are associated to active faults and were likely seismically triggered.

3. Data sources

The *SW* Iberian margin covers an area of approximately 458,400 km^2 from 33°0′ to 38.7°0′N and from 15.6°0′ to 6°0′ W, including the coasts of Spain, Portugal and Morocco. Available data for the area include a digital elevation model (DEM) (Fig. 1) constructed from multibeam bathymetric data (spatial resolution 115x115 m) that was collected in a total of 19 cruises from different European institutions (Zitellini et al., 2009) and compiled as part of the EMODnet bathymetry initiative (EMODnet Bathymetry Consortium, 2018).

The fault database used in this study is the European Database of Seismogenic Faults (EDSF; Basili et al., 2013). This database includes faults that are deemed to be capable of generating earthquakes of magnitude equal to or larger than 5.5 M_w and contains fault plane geometry information and a series of fault parameters such as strike, dip, rake, slip and earthquake magnitude information. In this study, the database was restricted to include only faults whose possible quake epicenters are mostly located offshore. This criterion is in line with that applied in the evaluation of probabilistic seismic hazard in the offshore scenario for structures in Portugal (Costa et al., 2008; Sousa and Oliveira, 1997).

A continuously updated landslide catalogue for the *SW* Iberian margin is being compiled at the Institute of Marine Sciences (CSIC) of Barcelona, systematically gathering previous data in the area (e.g., Baraza et al., 1999; Pajarón et al., 2015; Gràcia and Lo Iacono, 2008; Leon and Somoza, 2011; Mulder et al., 2009; Hanquiez et al., 2007). An earlier version of this catalogue is presented in Urgeles and Camerlenghi (2013). The landslide inventory includes information on typology, area, volume, thickness and depth of failure initiation.

Geotechnical data for the *SW* Iberian margin was gathered from different sources. Site location, water depth, and type of measurements are listed in Table 1; referenced locations are reported in Fig. 1.

4. Methodology

4.1. Overview

A dedicated GIS project was built for this study. Bathymetric data from the Gulf of Cadiz as well as information on submarine landslides, faults and geotechnical properties from the various databases were all imported into it. Operations within the GIS project are implemented using Python scripts with all input and output based on grid cells that represent 1 *km* x 1 *km*. Grid resolution was selected as a compromise amongst physical relevance, computational efficiency and possible loss of information due to averaging (Rodriguez-Peces et al., 2011).

A Montecarlo procedure (MC) is employed to obtain probabilistic landslide susceptibility maps using two different geotechnical slope stability assessment models. Two key aspects of the Montecarlo method are the selection of the stochastic inputs and the definition of probability density distributions for those inputs. In this work the stochastic input variables selected are slope gradient (α), horizontal peak ground acceleration (*PGA*) and two geotechnical variables (i.e. normalized undrained shear strength $\frac{Cu_{mobilised}}{\sigma'_{v0}}$ and normalized soil unit weight $\frac{\gamma}{\gamma'}$). In the precedent, $Cu_{mobilised}$ represents mobilized undrained shear strength, σ'_{v0} effective vertical stress, γ, total soil unit weight and γ' effective soil unit weight. All the stochastic inputs are represented through density distributions that are different at each cell of the map. From these individual cell distributions random samples of the stochastic variables are drawn at each run.

To set up the individual cell distributions different procedures are employed, because the nature of the uncertainties represented is also different. The information available on slope gradient (i.e. bathymetric) is exhaustive in its coverage, but affected by measurement error. The probability distribution that accounts for this uncertainty can be set up once and for all at each cell.

Local -i.e. cell- distributions of *PGA* represent uncertainties in earthquake magnitude at the source and attenuation due to varying distance to the source. Assuming that the source catalogue (the EDSF; Basili et al., 2013) is also exhaustive, these effects can be computed and a *PGA* distribution set up once and for all at each cell. Note that any limitations of the source database (e.g. its completeness) add a layer of uncertainty to the results, which is not explicitly represented in the model.

When addressing the uncertainty in geotechnical parameters the situation is different. Each 1 km^2 cell may be thought of as representing a "geotechnical site". At that cell-size, inherent ground variability in a site, even within the restricted soft soil classes assumed by the geotechnical models, is always significant Dreyfus et al. (2013). That local variability is what is directly represented by the parameter distributions set up at each cell. However, this opens up the question of how to choose the statistics of those local distributions, since the regional geotechnical database is very sparse.

The answer given is to combine the available regional information with that contained in global databases to set up a regional-scale distribution of plausible statistics to describe geotechnical site variability. At each cell in the map any of these plausible geotechnical sites is something that is assumed to be random. Therefore, two levels of sampling are needed in each Montecarlo round to initialize geotechnical model inputs. First, the statistics for the cell distributions are selected or, in other words, a plausible "geotechnical site" is assigned to each cell. Afterwards those local distributions are themselves sampled to obtain parameter values.

Once cell input distributions are initialized (i.e., at each grid cell density distributions of $\frac{Cu_{mobilised}}{\sigma'_{v0}}$, $\frac{\gamma}{\gamma'}$, α, *PGA* are defined), they are sampled at each simulation to obtain single values of slope gradient, *PGA*, normalized sediment density and normalized undrained shear strength (Fig. 2). Using these inputs two slope stability models are computed at each cell in each run.

The first slope stability model represents seismic loading as a quasi-static action, but with quasi-static coefficients calibrated using permanent-displacement Newmark-type analyses (Rampello et al., 2010). The Montecarlo output, at each grid cell, is a lognormal distributed pseudo-static factor of safety $FS_{p-stat.}$. The probability of failure P_f is simply evaluated as the number of simulated FS_{p-stat} lower than 1 over *N* simulations. Fig. 2a summarizes the workflow for this model.

In the second approach, the outputs are seismically induced Newmark displacements (Newmark, 1965), which are estimated using regressions with seismic ground motion, slope and geotechnical characteristics (Jibson, 2007). Direct application of the Newmark approach is computationally demanding for large-area mapping purposes and different indirect methods are used instead (Jibson, 2011). The Montecarlo output for each grid cell is a Newmark displacement probability density function PDF (D_n), which is also fitted to a lognormal distribution. This distribution may be used to compute exceedance probabilities for any chosen displacement D_n threshold (i.e. $P_{exceedance\ Dn}$). Fig. 2b summarizes the workflow for this model.

4.2. Slope stability assessment models

4.2.1. Pseudo-static approach

The pseudo-static approach is frequently used for regional landslide hazard mapping (Jibson, 2011). In this approach, an equivalent seismic coefficient k_h is introduced within a conventional limit equilibrium analysis. The infinite slope stability model can be expressed as (Lee and Edwards, 1986; Morgenstern, 1967):

Table 1
Summary of geotechnical data and methodology of acquisition of geotechnical data.

Type of data	Site Location	Cores	n° of data**	Water and subsurface depth information	Lithology description	Measurement methodology
$\frac{C_u}{\sigma'_{v0}}$	Continental margin of Gulf of Cadiz. Cores location: failed upper slope; stable upper slope; shelf mud-layer. Lee and Baraza, 1999, Fig. 1	37	118	From 30 m to 800 m water depth (cores up to 250 cm length from seabed)	Thin upper sand layer overlying a grayish olive, massive mud unit with bioturbation interlayered by silt unit mud-layer.	Vane shear measurements on the end of sections and for some split cores at 10-cm intervals.
	Marquês de Pombal landslide. Cores location: Head scarp; Landslide body; Most distal lobe. Minning et al., 2006, Fig. 1	4	287	From 2700 m up to 4000 m water depth (cores up to 520 cm length from seabed)	Mostly composed by silt and clay content with small sand fraction.	Fall cone penetrometer (Wykeham Farrance WF 21600) at 5-cm distance.
$\frac{\gamma}{\gamma'}$	ICM - 2018INSIGHT cruise Cores location: Lower slope (Fig. 1)	10	25	From 930 m up to 2667 m water depth (cores up to 268 cm length).		Handheld vane shear measurements
	Continental margin of Gulf of Cadiz. Cores location: Failed upper slope; Stable upper slope; Shelf mud-layer. Lee and Baraza, 1999, Fig. 1	7	14	From 30 m to 800 m water depth (cores up to 250 cm length from seabed)		Derived from water content
	Marquês de Pombal landslide. Cores location: Head scarp; Landslide body; Most distal lobe. Minning et al., 2006, Fig. 1	4	174	From 2700 m up to 4000 m water depth (cores up to 520 cm length from seabed)		Quantachrome pentapycnometer on 5 cm³ samples.
	Expedition 339: Gulf of Cadiz-W Iberian margin (Stow et al., 2013).					
	U1385 (Fig. 1) Borehole location: SW Iberian margin	67	60	Up to 150 mbsf*	Uniform lithology composed mostly by bioturbated calcareous muds and calcareous clays	Water content measurements on core specimens of 8 cm³. Volume of specimens measured by gas pycnometry.
	U1386 (Fig. 1) Borehole location: Continental margin of Gulf of Cadiz: middle slope ~ 25 km south-southeast of the Portuguese city of Faro. Middle-slope contourite deposits	18	197	Up to 586 mbsf*	Nannofossil mud, calcareous silty mud, and silty bioclastic sand lithologies	
	U1387 (Fig. 1) Borehole location: Continental margin of Gulf of Cadiz: middle slope, companion to Site U1386	86	275	Up to 870 mbsf*	Nannofossil mud, calcareous silty mud, and silty bioclastic sand lithologies generally organized as bi-gradational sequences.	
	U1388 Borehole location: This site is the site closest to the Strait of Gibraltar gateway.	24	47	Up to 1550 mbsf*	Strongly heterogenous media mostly composed by silty mud, calcareous clay, sand, silty sand.	
	U1389 Borehole location: ~ 90 km west of the Spanish city of Cádiz. Site in the "channels and ridges" sector of Cadiz margin.	107	278	Up to 990 mbsf*	Calcareous mud, silty mud, sandy mud, and silty bioclastic sand lithologies.	
	U1390 Borehole location: Second of two sites drilled in the channels and ridges sector of Cadiz margin.	38	121	Up to 350 mbsf*	Calcareous mud, silty mud, sandy mud, and silty bioclastic sand lithologies	
	U1391 Borehole location: 50 km northwest of Cape São Vicente, gently inclined middle-slope region.	56	188	Up to 672 mbsf*	Calcareous mud with minor lithologies including silty mud, sandy mud, nannofossil mud, and biosiliceous mud clayey foraminiferal nannofossil ooze.	
		Total 5447 m	Total 1166			
	DSDP Leg 79-546,79-545: Hinz et al., 1984, Fig. 1	60	76		Clayey foraminiferal nannofossil ooze. Firm clayey foraminiferal nannofossil ooze. Green nannofossil claystone. Grayish red sandy mudstone and muddy sandstone, pebbly at base.	GRAPE (Gamma Ray Attenuation Porosity Evaluation)

4

Table 1 (continued)

Type of data	Site Location	Cores	n° of data**	Water and subsurface depth information	Lithology description	Measurement methodology
	DSDP 14-135: (Hayes et al., 1972)	7	20		Top unit is comprised of Nannoplankton chalk ooze Pleistocene, Pliocene terregineous sediment with some silicified intervals and marl or limestone at the base.	GRAPE (Gamma Ray Attenuation Porosity Evaluation) Measurements at 0.5 cm interval.
	ICM - 2018 INSIGHT cruise *Cores location:* Lower slope (Fig. 1)	13	2137	From 930 m up to 2667 m water depth (cores up to 500 cm length).	–	GRAPE (Gamma Ray Attenuation Porosity Evaluation) Measurements at 0.5 cm interval.

* mbsf: length of all drill string components between sea floor and target.

** the number of data reported are referred to the ones above 350 m depth from seabed.

$$FS_{p-stat} = \frac{Cu}{\gamma'z \left[\, sin\alpha cos\alpha + k_h \, \frac{\gamma}{\gamma'} \, cos^2 \alpha \right]} \tag{1}$$

with:

α: slope gradient;

$\frac{Cu}{\gamma'z}$: normalized undrained shear strength.

$\frac{\gamma}{\gamma'}$: normalized sediment unit weight;

k_h: horizontal acceleration coefficient.

The horizontal acceleration coefficient is obtained as:

$$k_h = \eta \cdot PGA \tag{2}$$

where the coefficient η is applied to obtain a performance-based value of k_h.

Values of η coefficients used here are taken form the work of Rampello et al. (2010). Following a well-established methodology (Bray and Rathje, 1998; Stewart et al., 2003), Rampello et al. (2010) provided a suite of η values by correlation with the output of stochastic permanent-displacement Newmark type analyses. Different η values are obtained for different levels of Newmark displacement D_n values and for different site conditions. In this work the η values used are those associated to 15 *cm* permanent Newmark displacement for subsoil conditions described as loose-to-medium cohesionless soil and/or soft-to-firm cohesive soil (see Bisch et al., 2012). Newmark displacement values are used as indicative thresholds at which slope failure might occur (Jibson et al., 2000). Table 2 shows that resulting η values are slightly dependent on *PGA* values. All Newmark analyses in Rampello et al. (2010) used an Italian strong-motion database (Scassera et al., 2009) resulting from records generated by shallow crustal earthquakes with $Mw > 3.7$. Lacking more specific studies for the *SW* Iberian margin, η values derived from the Italian database were considered as appropriate for the *SW* Iberian margin.

4.2.2. Displacement-based approach

In the Newmark method the slide mass is represented as a rigid block (Newmark, 1965). In absence of inertial forces, the stability of the block is given by the static factor of safety FS_{stat}, here computed as:

$$FS_{stat} = \frac{Cu}{\gamma'z \; sin\alpha cos\alpha}; \tag{3}$$

with $\frac{Cu}{\gamma'z}$ and α previously described in eq. 2. Due to the seismic shaking, the critical acceleration, defined as the one that allows the block to glide (i.e., $FS_{p-stat} = 1$ in eq. 2) is then expressed as:

$$a_c = (FS_{stat} - 1)\tan(\alpha)\frac{\gamma'}{\gamma}g; \tag{4}$$

Given an earthquake acceleration time history, values in excess of a_c are applied to the failing mass. Two integrations of the filtered acceleration history results in a cumulative permanent displacement of the sliding block relative to its base. The method used here (Jibson, 2007) evaluates Newmark displacements from correlation with a ratio between the critical acceleration of eq. 4 and PGA:
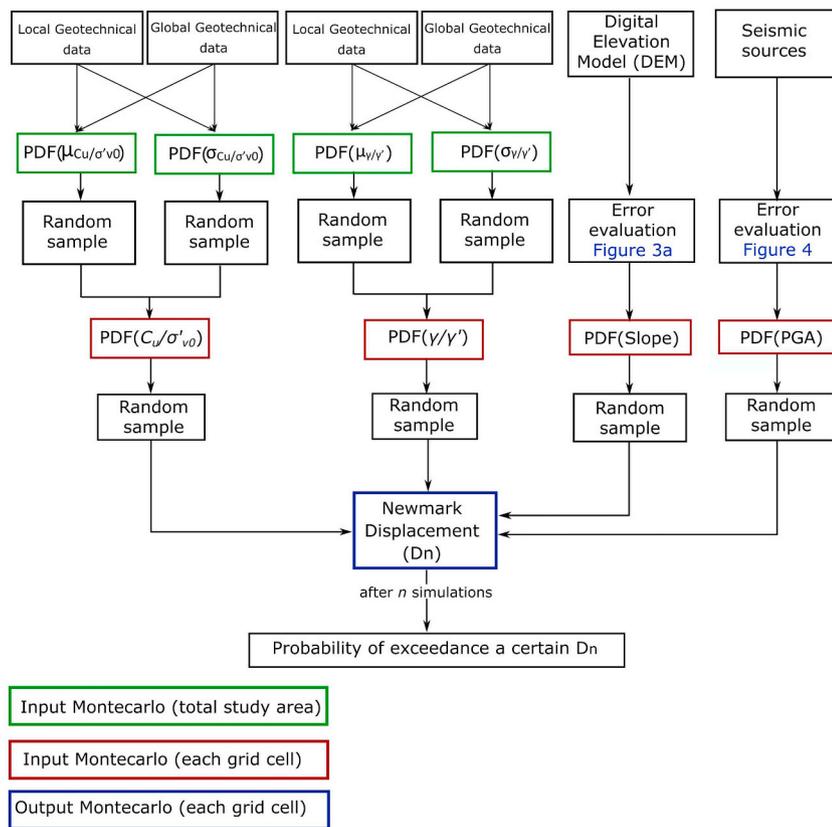
$$log_{D_n} = 0.215 \cdot log\left[\left(1 - \frac{a_c}{PGA}\right)^{2.341} \left(\frac{a_c}{PGA}\right)^{-1.438} \right] + \varepsilon_{\log(D_n)} \tag{5}$$

where:

D_n: Newmark permanent displacement [*cm*];

a_c: critical acceleration in *g*;

$\varepsilon_{\log(D_n)}$: model uncertainty, given by a normal distribution $N(0, \sigma_{\log(D_n)})$, with a standard deviation $\sigma_{\log(D_n)} = \pm 0.51$;

PGA: horizontal peak ground acceleration in *g's*, which accounts for soft sediments ground motion amplification effects.
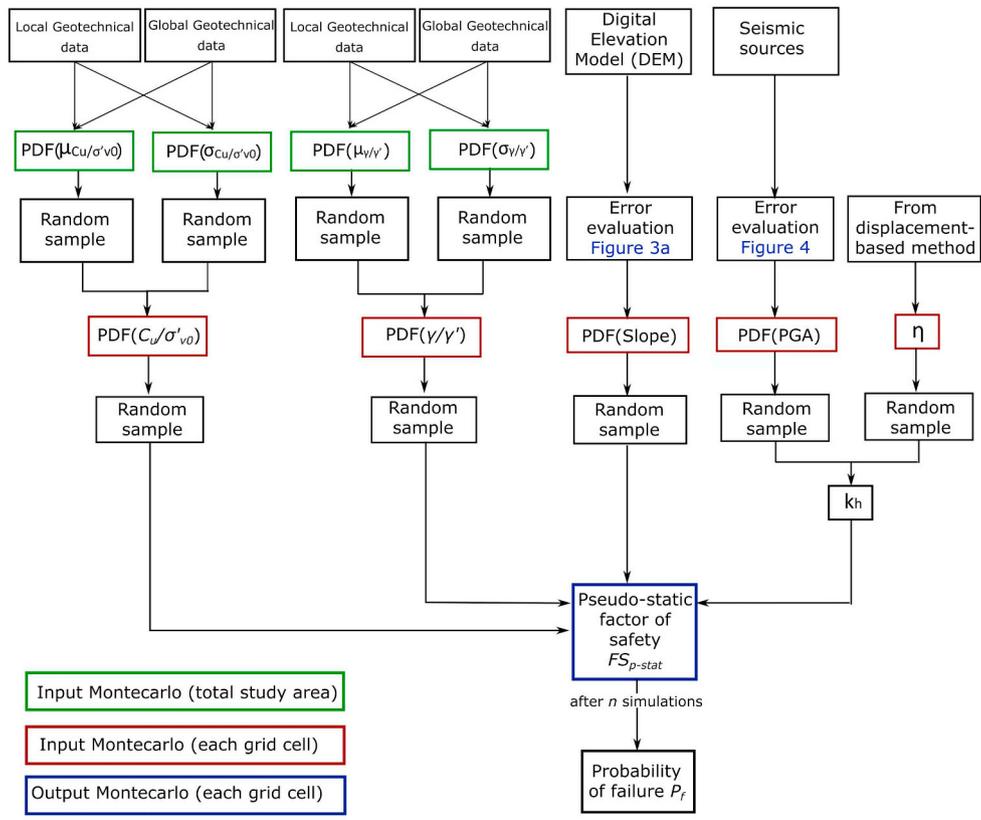
Fig. 2. a) Flow chart for pseudo-static slope stability probability model. b) Flow chart for displacement-based slope stability probability model.

Table 2

η values associated with 15 cm permanent displacements in soft-medium soils for different expected Horizontal Peak Ground Accelerations (Rampello et al., 2010).

Horizontal Peak Ground Acceleration (PGA) [g]	η
0.3–0.4	0.22
0.2–0.3	0.22
0.1–0.2	0.25
≤0.1	0.17

4.3. Treatment of model input uncertainties

4.3.1. Slope angle

Implicit in any DEM there is measurement error that propagates into slope angle uncertainty. Each multibeam system from which the DEM was obtained will introduce a slightly different error depending mostly on factors such as water depth, beam angle, bottom type and sea bottom geomorphology. As a consequence, the error in depth measurements would vary within a range of 0.04% to 0.15% for shallow water systems and from 0.2% to 0.5% for medium to deep water systems. A simplified approach has been taken in this study, and an average error value of 0.25% of the water depth is assumed throughout the DEM. Following Mudron et al. (2013), evaluation of the slope uncertainty in a DEM is quantified through a separate Montecarlo procedure (Fig. 3a). Assuming a normal distribution for the DEM error, with 0 mean and standard deviation $\sigma_{\varepsilon DEM}$ equal to 0.25% of the water depth, a randomly perturbed DEM is generated for each Montecarlo run (see example in Fig. 3b). The corresponding slope field is then evaluated using the 3×3 cell method as implemented in ArcGIS. After N simulations, a normally distributed slope angle is obtained for each cell. Convergence in slope statistics was observed after $N = 130$ simulations.

4.3.2. Horizontal peak ground acceleration

PGA values are usually derived from ground motion attenuation relationships, i.e. empirical correlations between maximum ground acceleration observed during an earthquake event at a given location and earthquake magnitude. The significant influence of magnitude in attenuation relationships is well recognized (Bommer et al., 2007). In particular, equations derived from large-magnitude events should not be extrapolated for prediction of ground motion from smaller events and vice versa. Mezcua et al., (2008) presented an attenuation relationship for the Iberian Peninsula, but cautioned against their use for

the Gulf of Cadiz, as it was largely based in smaller magnitude events compared to those expected there. In the Gulf of Cadiz, shallow crustal earthquakes associated to M_w greater than 5 are frequently recorded. For this reason, the PGA is evaluated using a more general approach proposed by Ambraseys et al. (2005), derived using Europe and Middle East large-magnitude events ($M_w > 5$). For soft soils this correlation reduces to:

$$\log(PGA) = 2.6595 - 0.142M_w + (-3.184 + 0.314M_w) \log \sqrt{d^2 + 7.6^2} \\ - 0.084F_N + 0.062F_T - 0.044F_O + \varepsilon_T \quad (6)$$

where:

$\log(PGA)$: logarithm of the horizontal peak ground acceleration $[ms^{-2}]$;

M_w: moment magnitude;

d: Joyner-Boore distance $[km]$ (i.e. distance to the surface projection of the fault);

$F_N = 1$ for normal faulting, 0 otherwise;

$F_T = 1$ for thrust faulting, 0 otherwise;

$F_O = 1$ for other styles of faulting, 0 otherwise.

ε_T: transformation uncertainty, modeled as- $N(0, \sigma_{\log(PGA)})$;

$\sigma_{\log(PGA)} = \sqrt{(0.665 - 0.065Mw)^2 + (0.222 - 0.022Mw)^2}$;

This relation introduces a small dependency on fault mechanism that is taken into account in our determination of the PGA, as the EDSF (Basili et al., 2013) includes such information for all faults. The coefficients to the terms F_N, F_T and F_O, imply that thrust faults will provide the most intense shaking compared to normal and strike-slip faults given an earthquake of the same magnitude (M_w) and at the same distance from the fault. The uncertainty introduced is clearly dependent on the M_w. For a magnitude range between 5.8 and 7.6, as for the case study, the uncertainty in ground motion prediction falls in the interval 0.31–0.18. The PGA for events in the upper range is therefore determined with somewhat higher accuracy.

For each fault, the catalogue provides 10 different estimates of maximum earthquake M_w derived from different correlations. In the EDS catalogue all these estimates are computed assuming full-length fault activation. The seismic events considered in this study as landslide triggers would then all be associated with relatively large return periods. Considering such long return periods is also justified by the submarine landslide catalogue used to validate the analysis. Even if the date of the events in this catalogue is not always well constrained, their position in the uppermost sedimentary sequences indicates that they are all Quaternary.
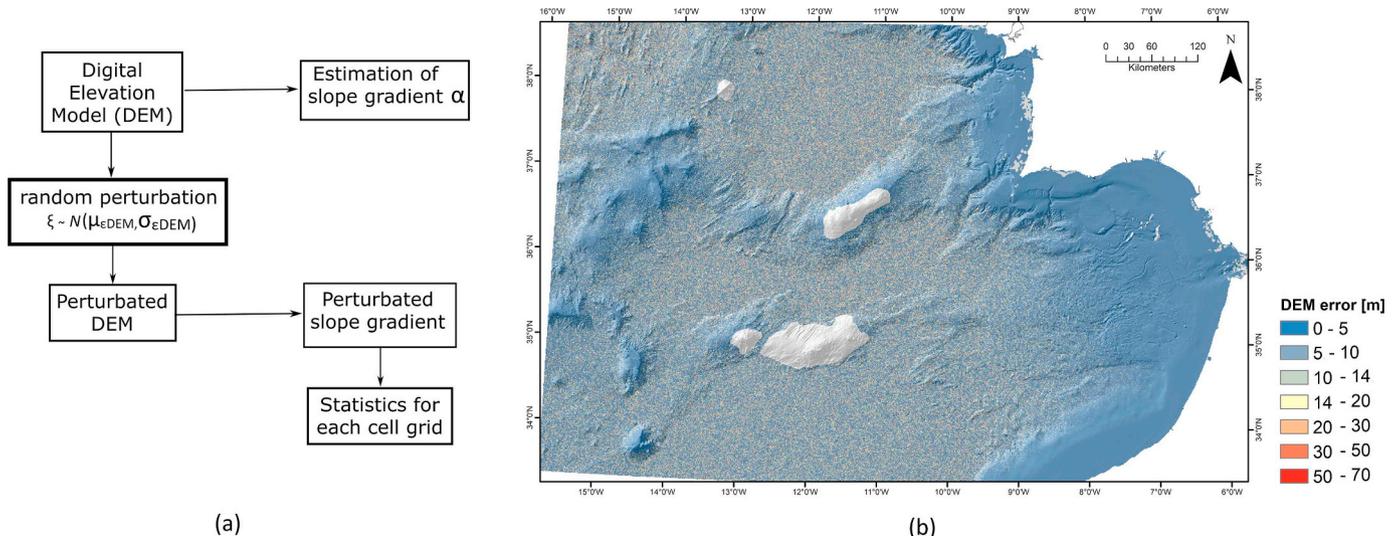

(a)   (b)

Fig. 3. a) Flow chart for slope uncertainty quantification, adapted from Mudron et al.,2013. b) Random DEM perturbation for ξ N (0,0.25% water depth). Axes show degrees latitude and longitude.
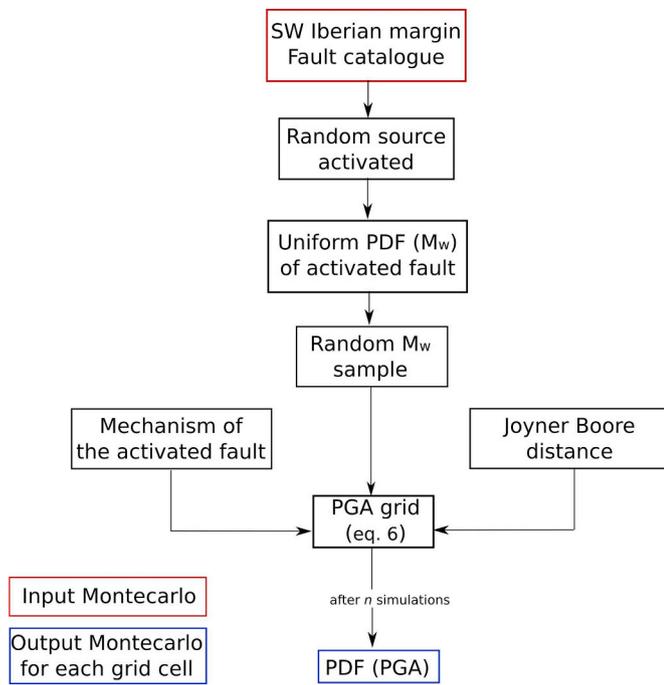
Fig. 4. Flow chart for PDF(PGA) and PDF(I_a) estimation.

Fig. 5. Example of ROC curve for landslide susceptibility model.

For each fault, the probabilistic description of M_w is given by a uniform distribution covering the entire range of estimates. As a result, uncertainty associated to the PGA at a site is given by the combination of that in the Ambraseys et al. (2005) correlation and that of the M_w.

Again, a separate Montecarlo procedure is employed to build a lognormal distribution of PGA values at each map cell. The main steps in the procedure are depicted in Fig. 4. At each simulation a random seismic source is activated. For such fault a random value of M_w is sampled from its uniform probability distribution to evaluate a PGA according to eq. 6 at all grid cells. The distribution statistics stabilizes after some 400 runs.

.

4.3.3. Geotechnical properties

The geotechnical information available for the study area is scarce. Some preliminary screening is possible: areas in which rock outcrops have been clearly identified (e.g. seamounts) are excluded from the analysis (Fig. 1). These areas appear as white spots in the maps (e.g. Fig. 3b). In addition to this, we assume that soft relatively fine sediments prevail, such that an undrained response to earthquake loading is plausible.

Given the large area (1 km^2) represented by each model cell, it is realistic to treat those as if they were different geotechnical sites. This, in turn, makes useful a conceptual scheme proposed by Zhang et al. (2004) in which the overall spatial inherent variability of geotechnical parameters is decomposed into within-site variability and cross-site variability. Within-site variability is embedded in the statistical

distribution assigned to a particular geotechnical parameter in a cell. Cross-site variability is represented by the variability of statistical parameters describing different local (i.e. cell-based) distributions.

For each of the geotechnical parameters involved X_D (i.e. sediment unit weight or normalized undrained shear strength) lognormal distributions at each cell are used to represent within-site variability. The first step in each Montecarlo run (see Fig. 2) is, then, to set up these distributions at each cell, i.e. to randomly assign a "site" to every cell in the model. To do so, statistical distributions of means and variances for the different geotechnical properties are sampled. Such statistical distributions of means and variances (i.e. of statistics) are themselves described as lognormal random variables.

The available data from the site investigations in the area (Table 1) provide a starting point to evaluate the density distributions for different geotechnical parameter statistics. However, given their non-uniform spatial distribution and reduced overall number, direct extrapolation to the whole area seems unwarranted. To circumvent this problem, a Bayesian framework is adopted to integrate this regional information with more general soil parameter information –i.e., a worldwide sourced database.

In the scheme adopted, information from the global databases is used to set up *prior* distributions for statistics of geotechnical parameters. Making use of Bayes' rule such *prior* information is then integrated with the SW Iberian margin regional data (i.e. *Data*) to obtain *updated* probability density functions (i.e. *posterior distribution*) of the relevant statistics, − the mean and standard deviations for the local distributions of geotechnical parameters. Following Straub and Papaioannou (2015), Bayes' rule for a generic random variable X is expressed as:

$$f''(x) = aL(x)f'(x) \tag{7}$$

where:

$f'(x)$ is the *Prior* probability density function for X.

$f''(x)$ is the *Posterior* or updated probability density function for X, taking into account the *Data*.

$L(x)$ is the likelihood or conditional probability of observing the Data when $X = x$,

Table 3
Statistical inputs to the Bayesian updating procedure of geotechnical parameters.

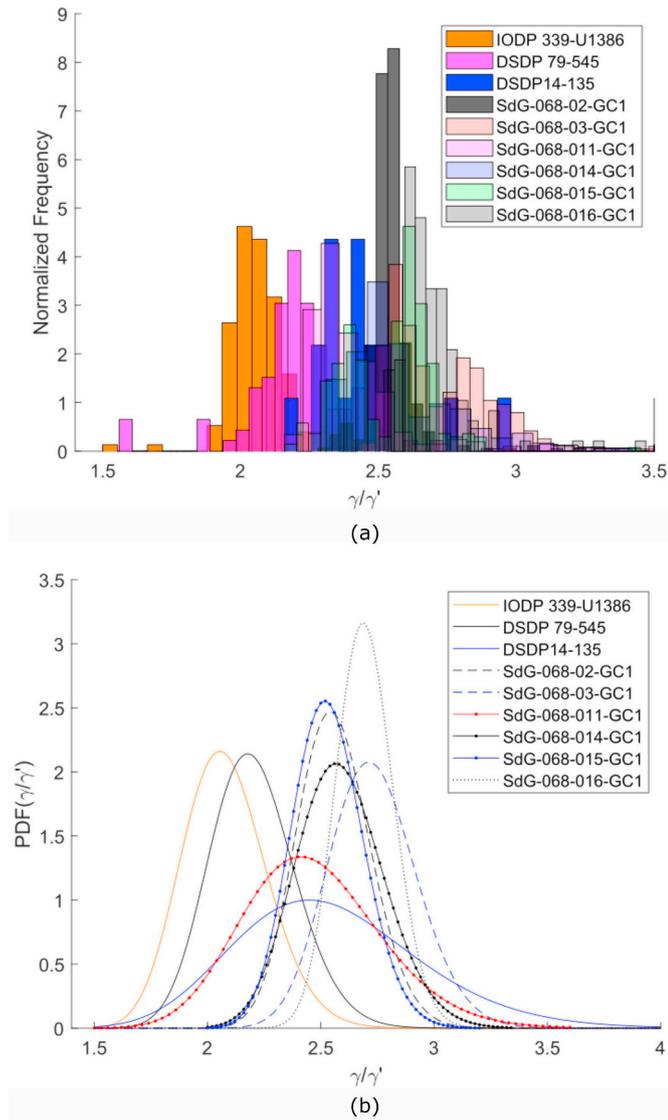|	$\sigma_{\varepsilon_{\mu T}}$ Error due to transformation of sediment strength from fall cone to vane test	$\sigma_{\varepsilon_{\mu\,Tw}}$ Weighted error (eq. 11)	Prior μ	Range μ	Prior σ_μ	Range σ_μ
$\mu_{\gamma/\gamma'}$	–	–	Uniform	[5.2–1.95]	Uniform	[0.4–0.1]
$\mu_{C_u/\sigma'_{v0}}$	0.0086	0.0048	Uniform	[1.45–0.1]	Uniform	[0.3–0.01]
	$\sigma_{\varepsilon_{\sigma T}}$	$\sigma_{\varepsilon\sigma_{T\_w}}$	**Prior μ_σ**	**Range μ_σ**	**Prior σ_σ**	**Range σ_σ**
$\sigma_{\gamma/\gamma'}$	–	–	Uniform	[0.75–0.02]	Uniform	[0.12–0.02]
$\sigma_{C_u/\sigma'_{v0}}$	0.4	0.22	Uniform	[1.75–0.1]	Uniform	[0.4–0.01]

(a)

(b)

Fig. 6. Normalized sediment unit weight data from the Gulf of Cadiz (a) histograms. (b) Adjusted PDFs.

(a)

(b)

Fig. 7. Histogram and prior distributions of normalized unit weight derived from the clay-offshore database plotted alongside the SW Iberian margin site data and deduced likelihood function for (a) the mean values and (b) the standard deviations.

Fig. 8. Liquid Limit-Plasticity Index (LL-PI) for the global dataset and Cadiz; Lee and Baraza,(1999).

$a = \frac{1}{\int_{-\infty}^{\infty} L(x)f'(x)dx}$ is a normalizing constant;

In this application, the random variables X are the statistics (mean and standard deviation) of the geotechnical parameters. The two geotechnical parameters used in the models, normalized sediment unit weight and undrained shear strength, are considered mutually independent. The *likelihood* function can be expressed as:

$$L(x) = P(Data \mid \mu_X, \sigma_X) = \prod_{i=1}^{Ns} \frac{1}{\sqrt{2\pi} \cdot \sigma_X} \exp\left\{ -\frac{1}{2} \cdot \left[\frac{\xi_i - \mu_X}{\sigma_X} \right]^2 \right\} \quad (8)$$

with:

$\xi_i =$ statistics from geotechnical data (i.e. logarithms of mean or standard deviations obtained at each regional site), computed from data reported in Table 1;

N_s: number of regional sites considered in the updating operation;

μ_X: logarithm of a possible mean for the variable X;

σ_X: logarithm of a possible standard deviation value for the variable X;

The Bayesian updating scheme is computed numerically. This is done using a Markov Chain Montecarlo (MCMC) method, using a Metropolis-Hasting algorithm implemented through a dedicated MATLAB script. The Montecarlo m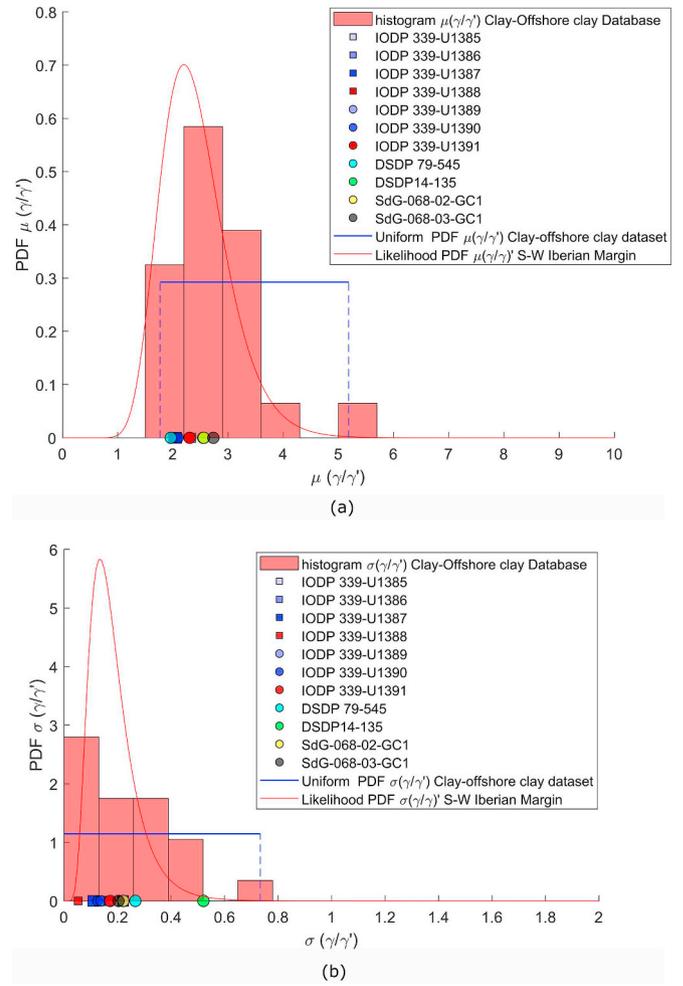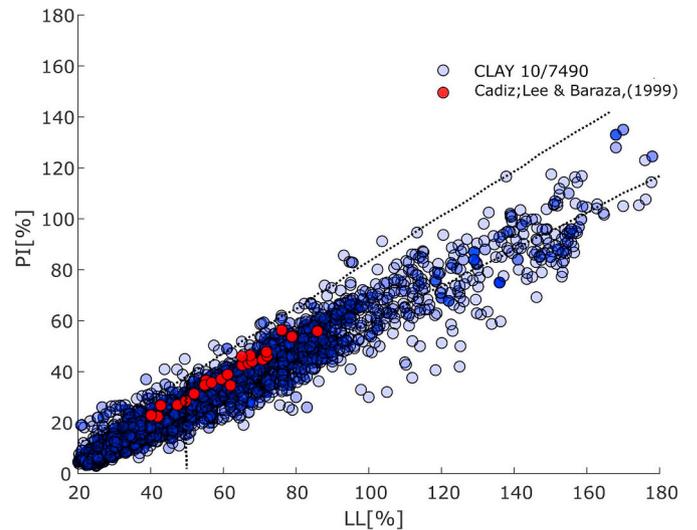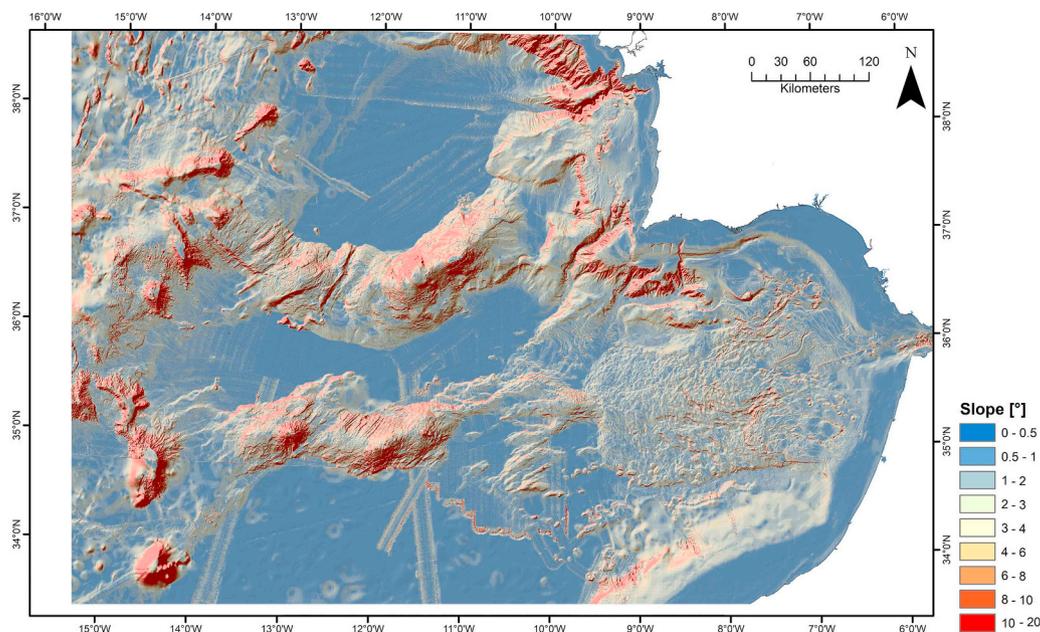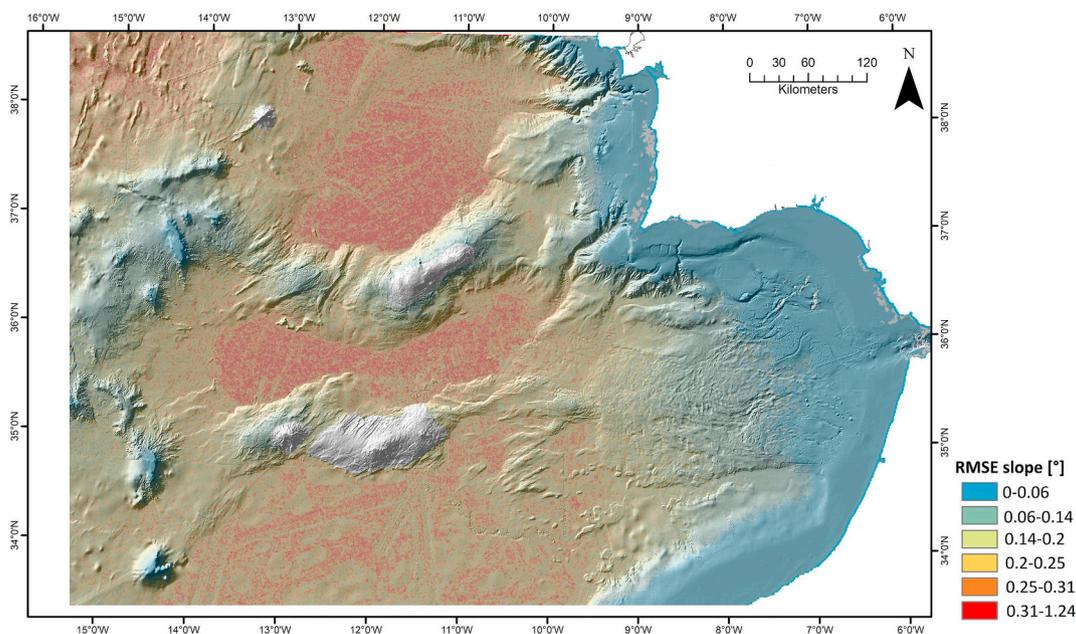ethod is used to obtain a probability distribution for the target parameter, sampling the prior distribution. To guarantee statistical robustness, this Montecarlo computation is repeated in sequence, setting up a Markov chain in which the posterior of

(a)

(b)

Fig. 9. a) Original slope gradient map. b) Slope RMSE map. Axes show degrees latitude and longitude. Black and white pixels represent rock outcrops.

the previous step is taken as new prior. See Wang and Cao (2013) for a detailed explanation of MCMC in a geotechnical context.

The computation of statistics at each site needs to account for different techniques used during data acquisition. In some cases, an empirical correlation was applied to transform the originally acquired data to a different strength measure (i.e. from fall cone test to vane shear strength). Such process adds a transformation error to the strength estimate. In such cases the original variability of a given dataset, represented by its standard deviation, $\sigma_{\xi 0}$, is increased by that of the transformation error, $\sigma_{\varepsilon T}$, to give (Phoon and Kulhawy, 1999a):

$$\sigma_{\xi} = \sqrt{\sigma_{\xi 0}^2 + \sigma_{\varepsilon T}^2} \tag{9}$$

The transformation error only affects part of the relevant collection of regional datasets. Therefore, a weighted average approach was used to account for this in the likelihood function:

$$\sigma_X = \sqrt{\sigma_{X0}^2 + \sigma_{\varepsilon T\_w}^2}$$

$$\sigma_{\varepsilon T\_w} = \frac{N_T}{N_{tot}} \sigma_{\varepsilon T} \tag{10}$$

with N_{tot} number of relevant data, and N_T number of data affected also by the transformation error.

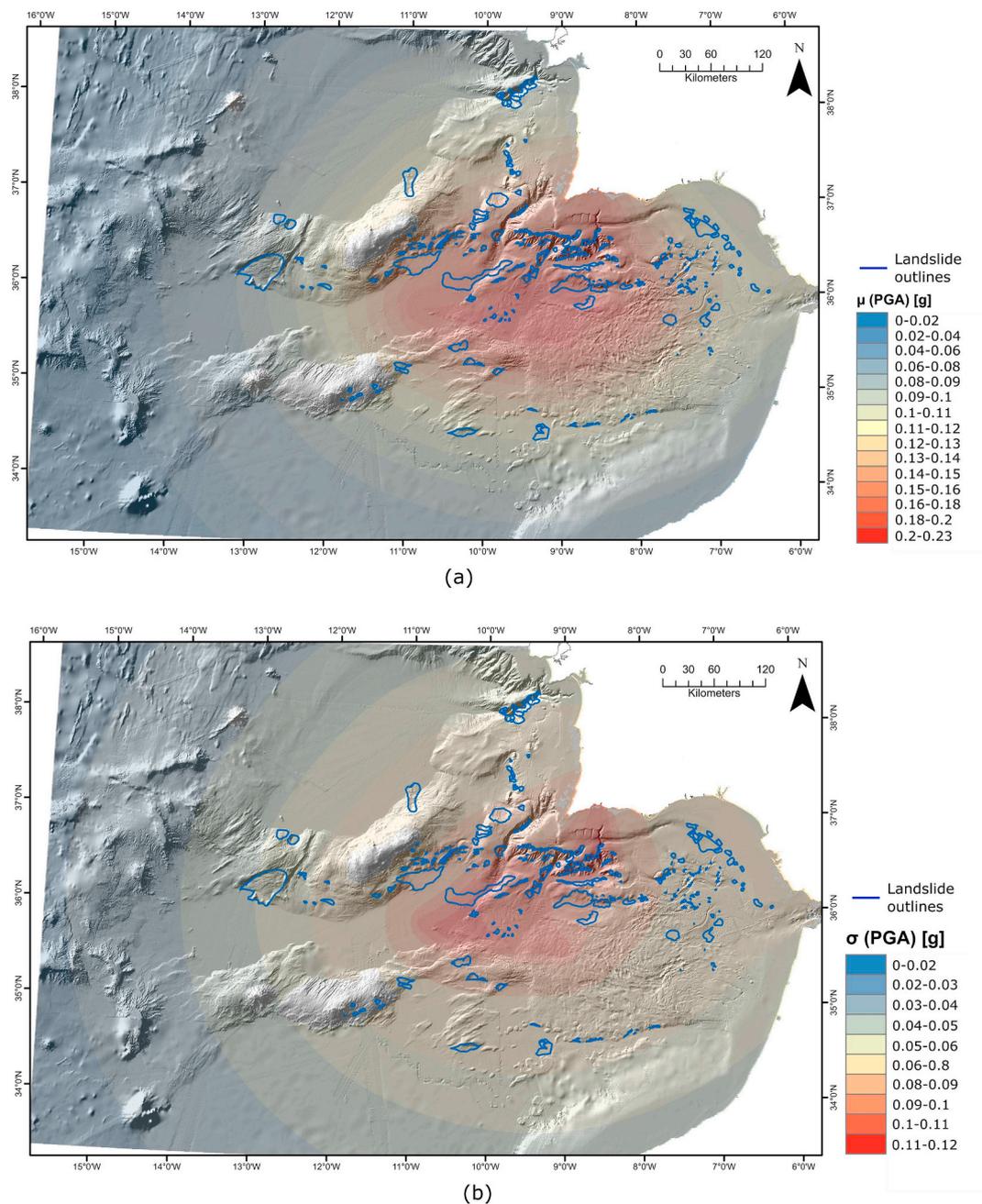*4.3.3.1. Normalized sediment unit weight.* Regional sediment density

Fig. 10. a) Local mean maximum PGA expected values assuming that the fault activates at full-length. b) Local PGA estimated variability.

measurements are obtained from deep *IODP* boreholes (Table 1), as well as from short core data from other sources. Data obtained in the *IODP* boreholes at depths below 350 m.b.s.f. was excluded, because that is the maximum excavation depth of landslides in the catalogue. Fig. 6a presents histograms of normalized sediment unit weight data from all available cruises that collected geotechnical data in the area. The values indicate significant variability within a range of 2 to 3.2, (equivalent to $14.55 \leq \gamma_{bulk} [kN/m3] \leq 20$). Fig. 6b presents adjusted lognormal distributions to the different datasets. From these adjusted curves a population of means and variances of site normalized unit weight is obtained. Normalized sediment unit weight (i.e. $\frac{\gamma}{\gamma'}$) was determined using a variety of methods (Table 1). However, we missed specific information on the statistics of conversion rules between the different methods employed to derive soil unit weight measurements, so they all were deemed equivalent and, as indicated in Table 3, no transformation was applied.

Mayne (2014) collected a global database of soil unit weights containing 1049 values representative of 88 sites with different soil types. Amongst those, sites representative of soft clays, offshore soft clays, offshore firm clays and offshore stiff clays were selected to build a new dataset (i.e., clay-offshore dataset), to be used as *Prior* Information in the Bayesian updating procedure. For each site in that restricted clay-offshore dataset the mean and variance of bulk density was estimated. Histograms of the means and variances thus obtained are depicted in Fig. 7a. The mean values in the clay-offshore dataset lie mostly in the range [1.9–3.97], except for some outliers. Considering now the standard deviations (Fig. 7b), it appears that within-site variability for the clay-offshore dataset lies generally below 0.4, with only a few outliers having larger values.

The offshore-clay normalized unit weight statistics are fitted with uniform prior distributions, illustrated in Fig. 7. It was decided to use the uniform distribution as *Prior* as it represents a less strong
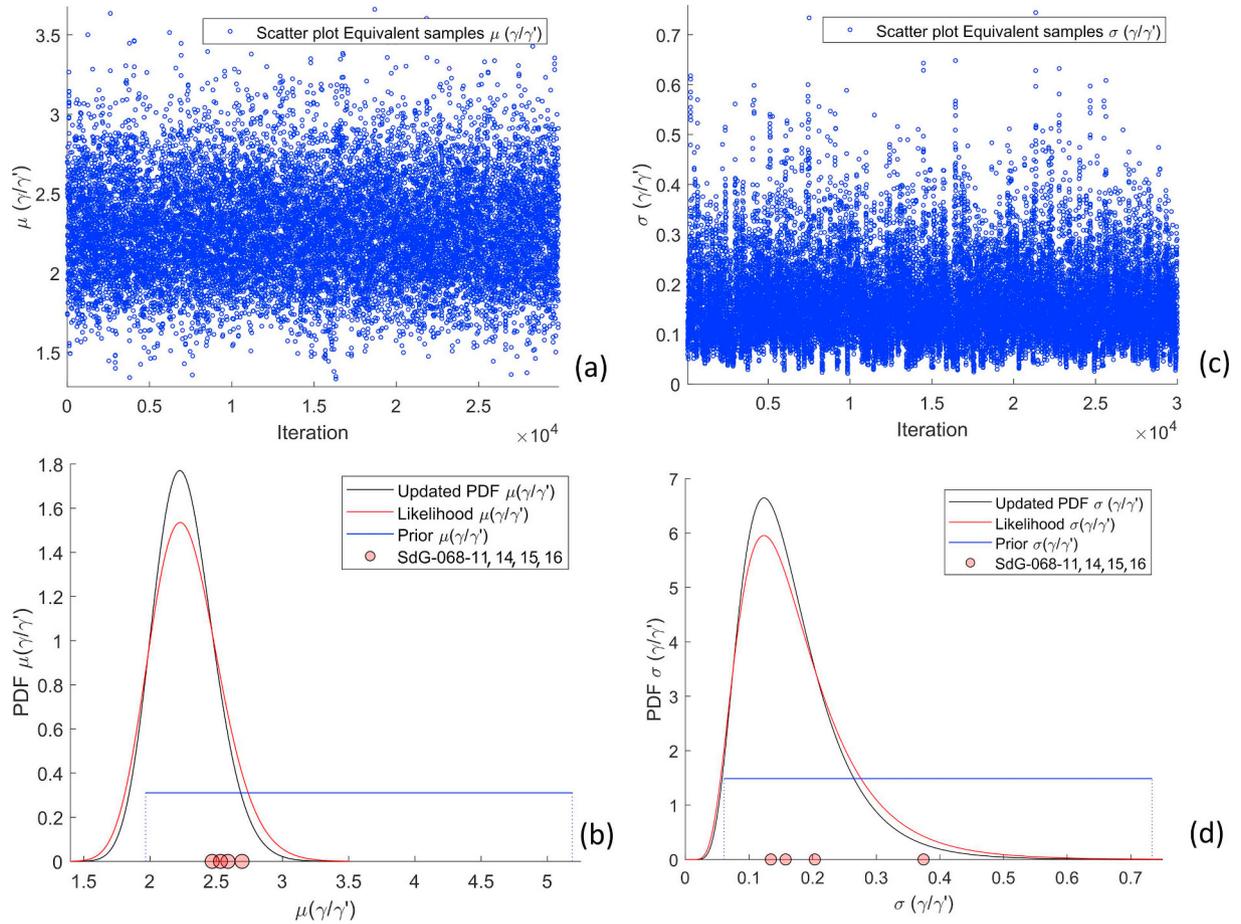
Fig. 11. a) Scatter plot of generated equivalent sample μ $(\frac{\gamma}{\gamma'})$. b) Updated PDF μ $(\frac{\gamma}{\gamma'})$. c) Scatter plot of generated equivalent sample σ $(\frac{\gamma}{\gamma'})$. d) Updated PDF σ $(\frac{\gamma}{\gamma'})$.

(uninformative) assumption (Table 3). Maximum and minimum values of statistics adopted in the uniform distribution are reported in Table 3. Regional data are also presented in Fig. 7 alongside a fitted lognormal distribution that will be employed to compute likelihood in the Bayesian update scheme.

4.3.3.2. Normalized undrained shear strength. When considering normalized undrained strength, the CLAY/10/7490 database (Ching and Phoon, 2014) is used to define the *prior knowledge*. Relevance of this *prior knowledge* was checked comparing regional data with the global dataset in terms of Liquidity index (*LI*) and Plasticity index (*PI*) (Fig. 8). This global database includes data from 251 sites. Normalized Cu_{vane} is considered herein as reference, since it closely corresponds to the strength mobilized in slope failures (Mesri and Huvaj, 2007). The range of statistics (mean and variance) of normalized Cu_{vane} data from the different case studies in the global database is used to define uniform *prior* distributions for the Bayesian updating procedure (see Table 3).

The regional undrained shear strength data from the SW Iberian margin sites is also dominated by vane strength measurements (e.g. Lee and Baraza, 1999). To consider also the fall cone measurements of Minning et al., 2006, a transformation is necessary. An empirical correlation for marine clays (Lu and Bryant, 1997) is used, namely

$$\mu_{Cu_{vane}} = 0.275\mu_{Cu_{fall-cone}} + \varepsilon_{\mu_T} \qquad (11)$$

where ε_{μ_T} represents the transformation error of the regression. This error is normally distributed with mean $\mu_{\varepsilon_{\mu_T}} = 0$ and $\sigma_{\varepsilon_{\mu_T}} = 0.0086$.

4.4. Assessment of model performance

To quantify the model performance, the model outputs (probabilistic susceptibility maps) are compared with the observations (i.e. grid cells with mapped landslide). Results of the comparison are expressed by means of Receiver Operating Characteristic (*ROC*) curves (Begueria, 2006; Frattini et al., 2010). *ROC* curves (Fig. 5) visualize model performance representing the True Positive fraction (TP) vs False positive fraction (FP) for given cut-off values (e.g. specified probability of failure value). TP is the proportion of positive cases correctly predicted by the model, while FP is the proportion of false positive (unstable grid-cells predicted as stable). Cut-off values are given by a certain probability of failure – for the quasi-static model- and for a certain displacement value – for the displacement-based approach. The area between the *ROC* curve and the diagonal in the graph (Area Under the Curve or AUC) gives a measure of potential discriminating power for the model, with more powerful models resulting in larger areas. Since the landslide catalogue used does not differentiate between source area and deposit (mostly spread on flat areas), only reported landslide grid-cells with slope angles greater than 3° are considered for model validation. This left 4007 cells available for model evaluation.

5. Results

5.1. Slope gradient statistics

As previously described, the slope root mean square error (RMSE) for each cell grid is a function of both water depth and slope angle magnitude. For a fixed ratio of bathymetric measurement uncertainty, the slope gradient error is inversely proportional to the magnitude of
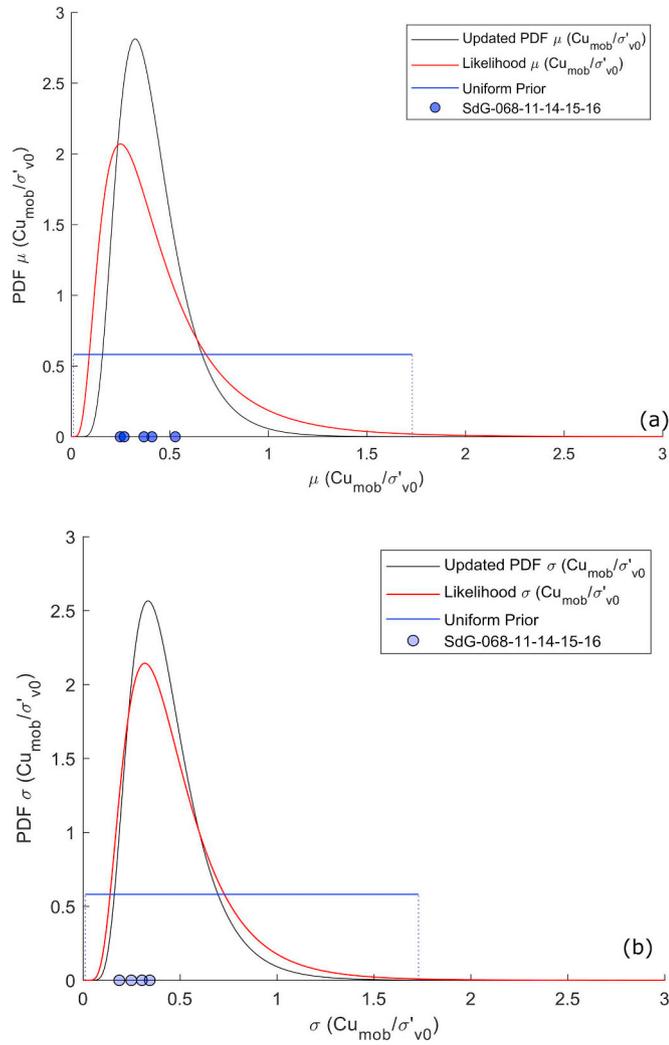
Fig. 12. a) Updated PDF($\mu_{\frac{Cu_{vane}}{\sigma'v0}}$). b) Updated PDF($\sigma_{\frac{Cu_{vane}}{\sigma'v0}}$).

the slope angle. Therefore, steep slopes in shallow water are evaluated with more accuracy than flat areas in deep water. Still, the absolute magnitude of this derived uncertainty is rather small. A maximum error of 1.28° is expected for flat areas, while in steep slopes the RMSE is rarely above 0.15° (Fig. 9).

5.2. Peak ground acceleration

Seismogenic faults incorporated in the Montecarlo procedure are labeled in Fig. 1. Fig. 10 reports the statistics (i.e. mean and variance) of the local probability distribution functions of the aggregated maximum *PGA* that these faults can deliver. The local mean μ_{PGA} is a function of the relative distance of the faults to the particular cell. This implicitly assumes a temporal dimension large enough so that all faults will be active at one moment or another along their entire length. The faults incorporated in the Basili et al. (2013) catalogue are all considered active faults and therefore such assumption is reasonable. A maximum mean value of 0.23 *g* is obtained for sites nearby the Horseshoe abyssal plain (i.e. Horseshoe fault Fig. 1). Along the Portuguese margin values between 0.15 and 0.13 g have been obtained. Such values are in agreement with those available in the current seismic hazard zonation for Portugal (Costa et al., 2008) for a similar seismic scenario and a probability of exceedance of 10% in 50 years (i.e. 475 years return period). The *PGA* variability, σ_{PGA} (Fig. 10b) is also greater in the proximity of the Horseshoe fault.

5.3. Normalized sediment unit weight

A total of sixteen regional data groups were available from which mean and variances of normalized unit weight distributions could be extracted. For this purpose, the information from deep boreholes in the Iberian margin (i.e., *IODP* Exp. 339 in Table 1) was split into seven locations, as the boreholes were performed at large distances from one another. As detailed in Table 4, the datasets from twelve sites were selected for the updating operation, leaving 4 aside for validation.

Fig. 11 presents the Bayesian updating results for the assumed prior uniform distributions of normalized unit weight statistics. The figures present the Equivalent Samples generated during the MCMC run, as well as the resulting updated distributions. Comparing likelihoods and updated distributions it can be seen that the Bayesian approach has been effective in reducing the spread of the distributions that will feed site statistics to the map cells. The most relevant distribution values are reported in Table 5. Finally, it may be noted that the validation data points lie unambiguously within the bounds of the updated distributions.

5.4. Normalized undrained shear strength

As indicated in Table 4, nine regional site datasets, out of the thirteen used to evaluate $\mu_{\left(\frac{Cu_{vane}}{\sigma'v0}\right)}$ and $\sigma_{\left(\frac{Cu_{vane}}{\sigma'v0}\right)}$, were used as input to the Bayesian updating procedure and four were reserved for validation. Results in terms of updated PDF ($\mu_{\left(\frac{Cu_{vane}}{\sigma'v0}\right)}$) and *updated* PDF ($\sigma_{\left(\frac{Cu_{vane}}{\sigma'v0}\right)}$) are presented in Fig. 12. The most relevant distribution values are reported in Table 5. Concerning $\mu_{\left(\frac{Cu_{vane}}{\sigma'v0}\right)}$ all the four validation data fall within the 90% inter-percentile range of [0.19–0.79]. A 90% inter-percentile range of [0.17–0.8] is derived instead for $\sigma_{\left(\frac{Cu_{vane}}{\sigma'v0}\right)}$, which also includes the four-validation data. Statistics of the Updated *PDFs* are reported in Table 5.
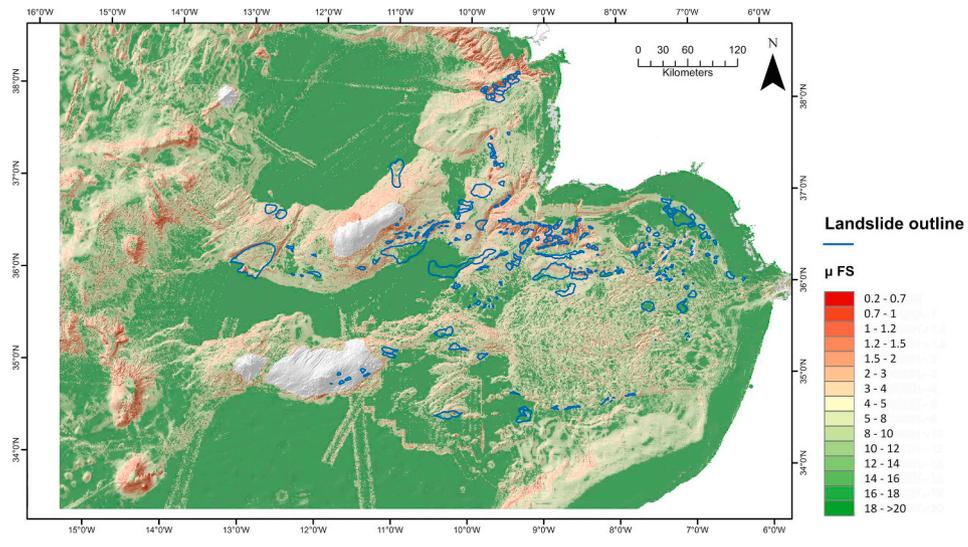
5.5. Landslide susceptibility map: pseudo-static approach

Having obtained the PDFs for all input parameters required by the seismic slope stability calculation the Montecarlo procedure in Fig. 2a was run. A total of 1000 simulations were performed to achieve a failure probability precision of around 0.01 (Wang et al., 2011). The local mean value of the pseudo-static factor of safety distribution is obtained and reported in Fig. 13a. As expected, lower values of factor of safety (i.e. slopes prone to failure) are associated to sites with high values of predicted PGA and slope gradient. A minimum value of 0.4 appears in the most susceptible areas (nearby Cape Sao Vicente, Marques de Pombal fault and Gorringe bank fault), while $FS_{p-stat} > 20$ are obtained for flat areas offshore the Iberian margin. The precision of the derived factor of safety is quantified by its local variability expressed in terms of the square root of the variance of FS_{p-stat} (Fig. 13b). The latter is given by the combination of morphological, geotechnical and PGA uncertainties.
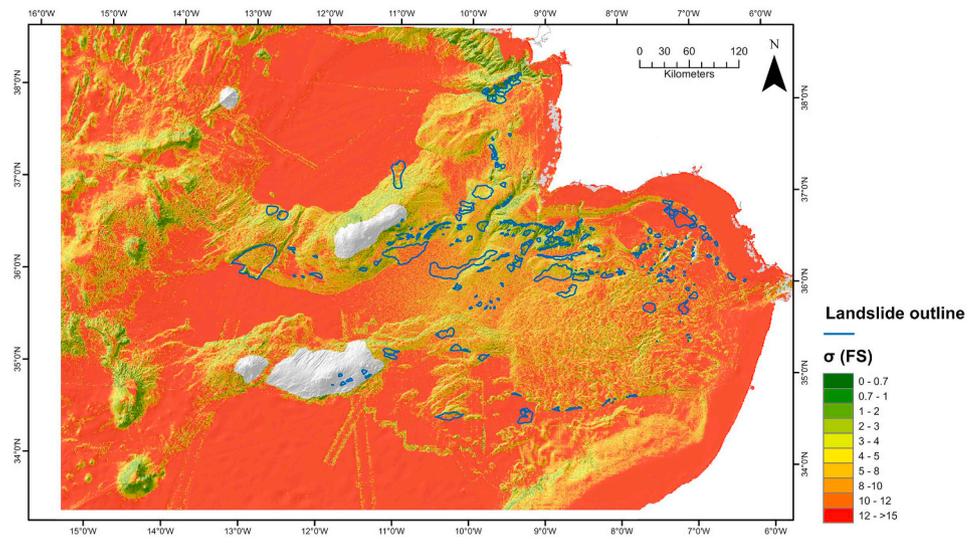
A noteworthy result is that uncertainty in the FS_{p-stat} decreases for low values of the *FS*. Therefore, unstable sites are quantified more precisely than stable ones. This is in apparent contrast with *PGA* results reported in Fig. 10, where higher uncertainties are associated to greater *PGA* values. A plausible explanation for this result may be obtained applying a first order second moment method (FOSM) derivation (Baecher and Christian, 2005) to the slope stability (Eq. 1). The contribution of seismic shaking to the overall FS uncertainty at each grid cell can be expressed as:
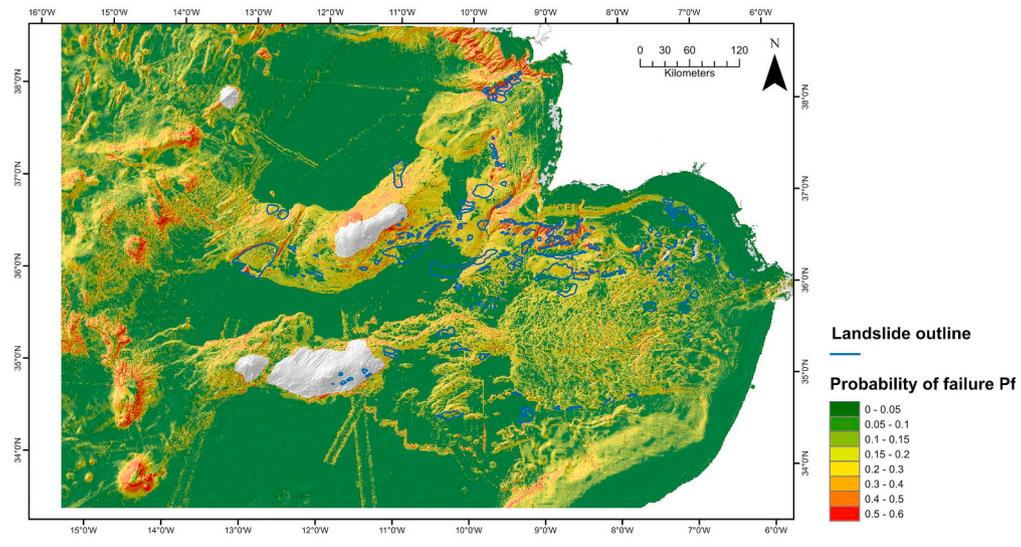
$$\sigma^2_{FS_{(k_h)}} = \frac{\overline{Cu}}{\gamma'z} \frac{1}{\left[\sin\overline{\alpha}\cos\overline{\alpha} + \overline{k}_h \frac{\overline{\gamma}}{\gamma'}\cos^2\overline{\alpha}\right]^2} \cdot \frac{\overline{\gamma}}{\gamma'}\cos^2\overline{\alpha} \cdot \sigma^2_{k_h}$$

(12)

where:

(a)

(b)

(c)

(caption on next page)

$\frac{\overline{Cu}}{\gamma'z}$: local (i.e. grid cell dependent) mean value of the normalized shear strength;

$\frac{\overline{\gamma}}{\gamma'}$: local mean value of the normalized sediment unit weight;

$\overline{\alpha}$: local mean value of slope angle;

$\overline{k_h}$: local mean value of the horizontal acceleration coefficient;

$\sigma_{k_h}^2$: local variance of the horizontal acceleration coefficient.

The mean value of local acceleration appears in the quadratic expression in the denominator of (Eq. 12). This value will overcome the effect of increased local variance $\sigma_{k_h}^2$ with acceleration magnitudes and result in a less uncertain prediction of the *FS*.

Similar observations apply to the probability of failure P_f, reported in Fig. 13c alongside the inventory of submarine landslides in the SW Iberian margin (blue outlines). P_f increases for steep slopes subject to high *PGA* (nearby Cape Sao Vicente, Marques de Pombal fault and Gorringe bank fault) with values up to 0.64, decreasing for rather gentle gradients.

5.6. Landslide susceptibility map: displacement-based approach

The displacement-based susceptibility map is derived following the steps reported in Fig. 2b, resulting, as previously explained, in log-normal distributions of D_n at each grid-cell. The main output cell statistics are reported in Fig. 14a and Fig. 14b alongside the landslide inventory (i.e. blue outlines). Predicted permanent displacement mean values μ_{Dn} range from 0 to 72 *cm*. Greater displacements are associated to sites characterized by steep slope gradients and high values of expected *PGA*. The uncertainty associated to D_n estimates is quantified by its standard deviation σ_{Dn} at each cell (Fig. 14b). This uncertainty closely reflects that of the seismic ground motion (see Fig. 10b). The D_n statistics may be employed to derive a probability of exceedance of a chosen D_n threshold (i.e. $P_{exceedance\ [Dn]}$), computed as 1-CDF ($D_{n-treshold}$). An example is illustrated in Fig. 14c, which reports the probability of exceedance of a D_n equal to 5.2 cm. The significance of this particular D_n value is best appreciated after considering the results of the model validation in the next section.

5.7. Model validation

As described in section 4.4, model performance is analyzed through the *ROC* curve. For the pseudo- static approach, the *ROC* curve is computed for different P_f cut-off values. For the displacement-based approach, a *ROC* curve is defined employing different D_n threshold values. In both cases *ROC* curves are computed using a random subset including 75% of the pixels catalogued as landslides (a raster layer containing ones, pixels containing landslides, and zeros). The remaining 25% are reserved for validation.

Fig. 15 shows that a slightly better performance is achieved by the pseudo-static approach. Indeed, the AUROC value (Area Under the Receiver Operating Characteristic) for the quasi-static model is 0.96 whereas the one computed for the displacement-based approach is 0.935. When compared with results of other landslide susceptibility mapping studies (e.g. Park et al., 2013; Goetz et al., 2015; Cantarino et al., 2019) our values indicate good accuracy for the models employed here. The *ROC* point that maximizes both specificity and sensitivity (i.e. maximum distance from the trivial model) may be used to identify an optimal threshold. An optimal point in the P_f equal to 0.22 is obtained for the pseudo static approach, while for the displacement-based analysis, a $D_{n-treshold}$ of 5.2 cm is obtained.

In the displacement-based analysis, the *ROC* curve can be also parametrized using exceedance probabilities. Using $P_{exceedance\ [5.2cm]}$ as input, the optimal point is given by $P_{exceedance\ [5.2cm]}$ equal to 0.135.

Therefore, $P_f = 0.22$ and $P_{exceedance\ [7cm]} = 0.135$ may be used as model output boundaries to classify susceptible and unsusceptible grid cells. These criteria were checked using the landslide subset randomly selected for validation. The results are summarized in Table 6. The quasi-static model predicts correctly 92% of the cells in the validation subset and the displacement-based method 82%.

6. Discussion

6.1. Limitations affecting the results

There are several strong assumptions inherent to the slope stability models that are at the core of the methodology presented in this study. From the geometrical viewpoint there is no clue in the model about the lateral extent or volume of the sliding mass. From the material viewpoint the models assume that the sliding mass is a soft sediment, normally consolidated, which would shear undrained when subject to seismic shaking. The assumption of normally consolidated material may not represent well the sediment strength and density profile in areas of significant erosion such as submarine canyons. With regard to in-situ stresses, it should be noted also that excess pore pressures induced by rapid sedimentation are not considered. Although in most marine deposits it is correct to assume that conditions are hydrostatic (Lee and Edwards, 1986), overpressure is possible in areas where the sedimentation rates are relatively high (e.g., Urgeles et al., 2006; Llopart et al., 2015). Alternatives to address these model limitations are outlined in section 6.3 below.

Other limitations to the results presented are inherent to the databases employed. In particular, the magnitude estimates in the European Database of Seismogenic Faults assume full-length fault dislocation. This assumption implies relatively large return periods for the ground shaking events. However, such long return periods are justified by the submarine landslide catalogue that is used to validate the analysis, as the date of the events in this catalogue is not well constrained in many instances but, because of their position in the uppermost sedimentary sequences, they can all be assumed to be Quaternary.

A strong limitation of the submarine landslide database employed is that it does not distinguish between source area and deposit. Because submarine landslides may travel long distances from the area that initially failed (e.g., Elverhøi et al., 2000; De Blasio et al., 2004) a database that identifies the landslide source area will be better adapted to highlight the factors linked to the failure without the influence of the landslide dynamics. The slope-angle based filtering criteria that has been applied to get around this limitation is a relatively crude solution.

6.2. Model performance

Despite all the limitations signaled above overall model performance, as measured by the *AUROC* curves, is noteworthy. This good performance suggests that, within the limits of the employed databases, seismic triggers are the dominant cause of submarine slope failure in the *SW* Iberian margin.

The (slightly) better performance of the quasi-static model should not come as a surprise. Both the quasi-static and the displacement-based approach applied here are ultimately based on statistical regressions of Newmark method outputs for a given set of input seismic motions and slope descriptors. In the displacement-based method that regression directly gives an estimated displacement, whereas in the quasi-static method the regression is used to establish the mobilization factor η. The statistical work of Rampello et al. (2010) is based on seismic motion records from Italy, which from a tectonic viewpoint is a
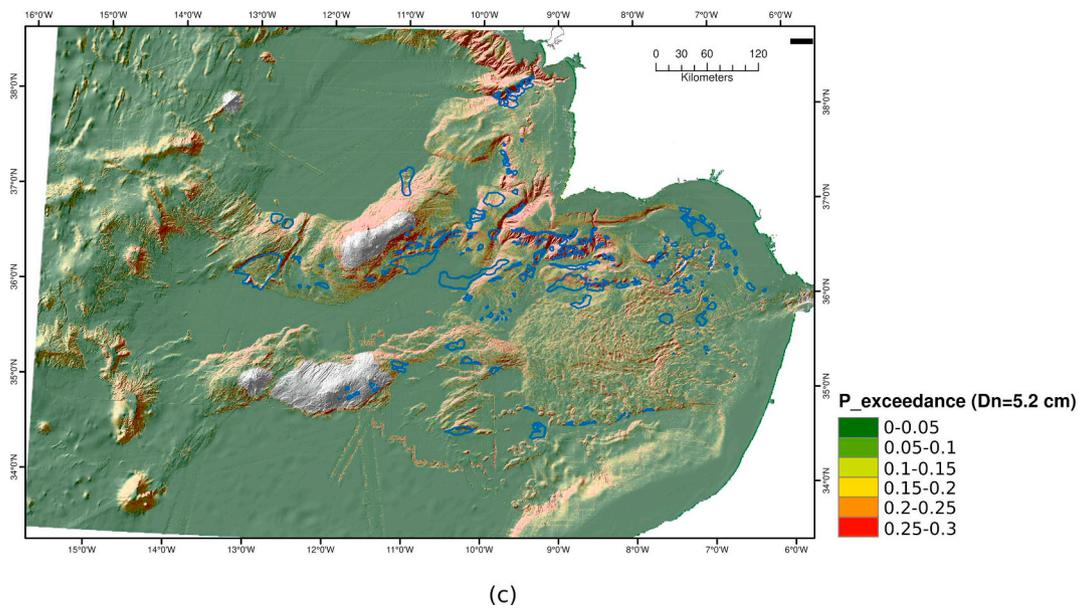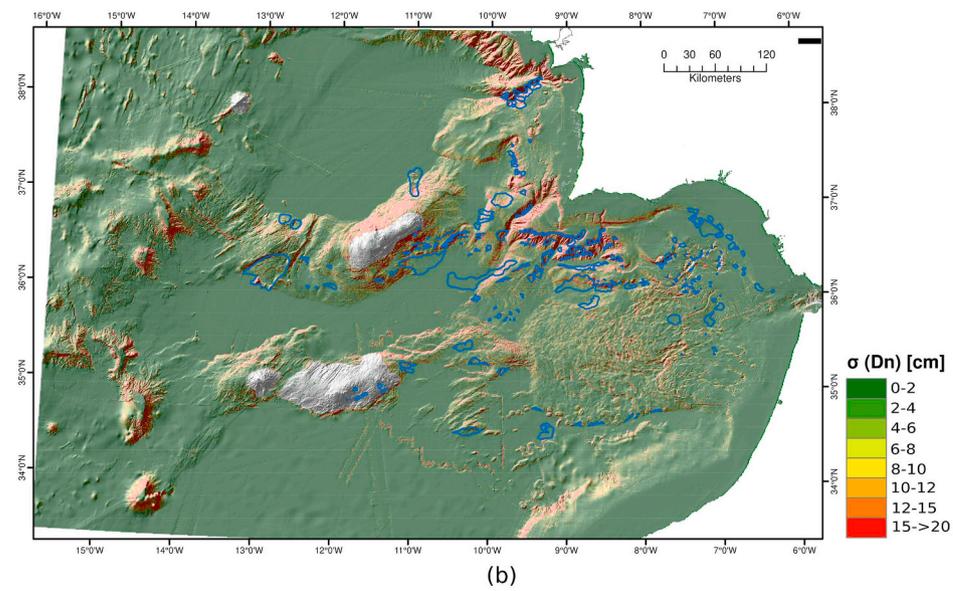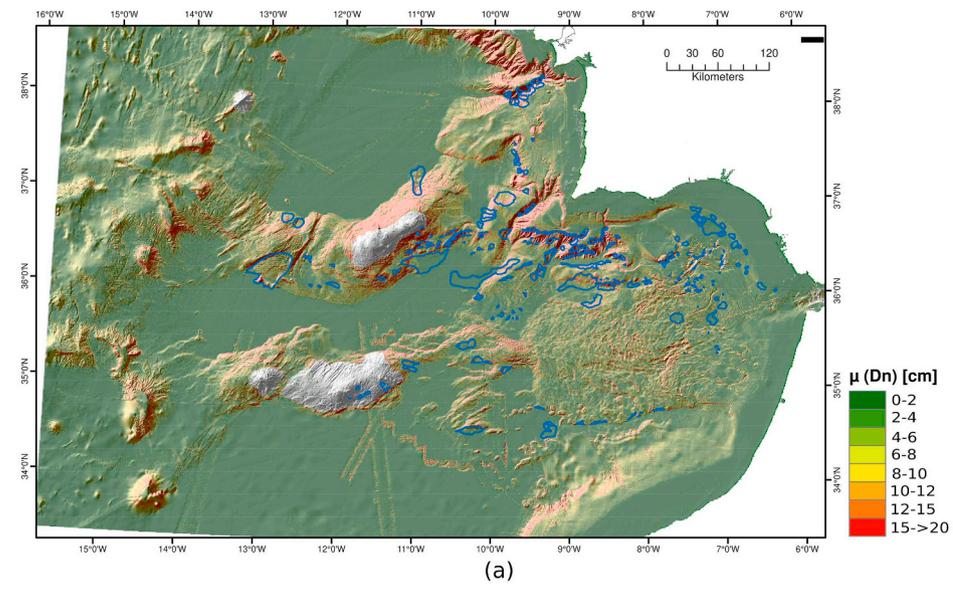
(a)

(b)

(c)

(caption on next page)
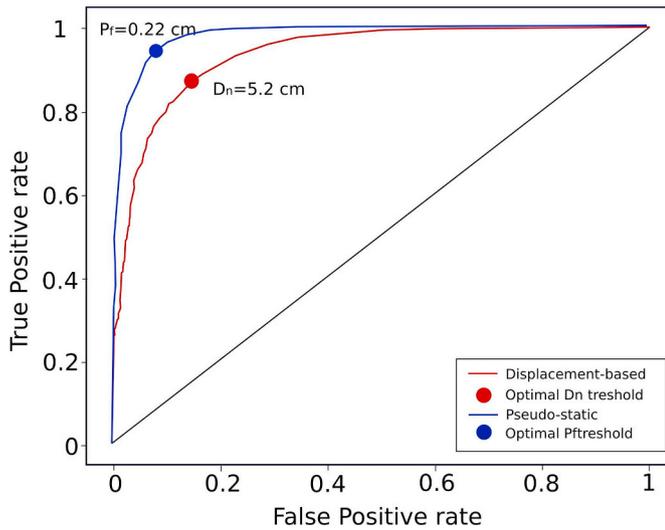
Fig. 15. *ROC* curve and Optimal thresholds for Pseudo-static model and Displacement-based method.

Table 4
Regional datasets employed as input and validation for the Bayesian updating procedure. SdG068-XX are measurements performed on samples collected in 2019 during the INSIGHT Leg-1 cruise. See Stow et al. (2013) for details of IODP Exp. 339 Sites.

Variables	Input data	Validation data
$\mu\left(\frac{C_u}{\sigma'_{v0}}\right); \sigma\left(\frac{C_u}{\sigma'_{v0}}\right)$	9 **Sites** - 4 sites Minning et al., 2006 - 3 sites, Lee and Baraza, 1999 - SdG068–02 - SdG068–03	4 SdG068–11 SdG068–14 SdG068–15 SdG068–16
$\mu\left(\frac{\gamma}{\gamma_s}\right); \sigma\left(\frac{\gamma}{\gamma_s}\right)$	12 **Sites** - IODP Exp. 339 U1385 - IODP Exp. 339 U1386 - IODP Exp. 339 U1387 - IODP Exp. 339 U1388 - IODP Exp. 339 U1389 - IODP Exp. 339 U1390 - IODP Exp. 339 U1391 - DSDP Leg 14–135 - DSDP Leg 14–79 - Minning et al., (2006) - SdG068–02 - SdG068–03	4 SdG068–11 SdG068–14 SdG068–15 SdG068–16

reasonable proxy for the Gulf of Cadiz. The displacement-based model performance might also be improved by using richer descriptions of seismic ground motion, for instance using models that also include Arias intensity within the predictor variables (Jibson, 2007).

The calibration of the quasi-static method using dynamic effects affects the performance of the method. Fig. 16 shows the estimated probability of failure using a non-calibrated reduction factor value frequently used in practice (i.e., $\eta = 0.5$). When compared with the calibrated method (Fig. 13c) the new results show a general increase in slope failure susceptibility.

Model performance should be reevaluated in the future, as the landslide catalogue is updated and becomes more precise. A particularly significant improvement in this respect may be a landslide catalogue that distinguishes between landslide source and landslide deposits. By using the polygons of the landslide source areas only, we will ensure that the input in the model performance and validation through the ROC curves will not be contaminated by portions of the polygons

where the slope stressors, factor of safety and probability of failure are not related to the slope failure conditions.

6.3. Enhancing the susceptibility maps

The susceptibility maps might be further enhanced if other conditioning factors are included. An additional input factor that could be considered is the occurrence of overpressure. In a first approximation this may be explored using very similar models. For example, following (Carlton et al., 2017) the pseudo-static slope stability model might be reformulated as:

$$FS_{p-stat} = \frac{Cu}{\gamma'z\left[\ sin\alpha cos\alpha + k_h\ \frac{\gamma}{\gamma'}\ cos^2\alpha\ \right]}\ (1 - r_u)$$
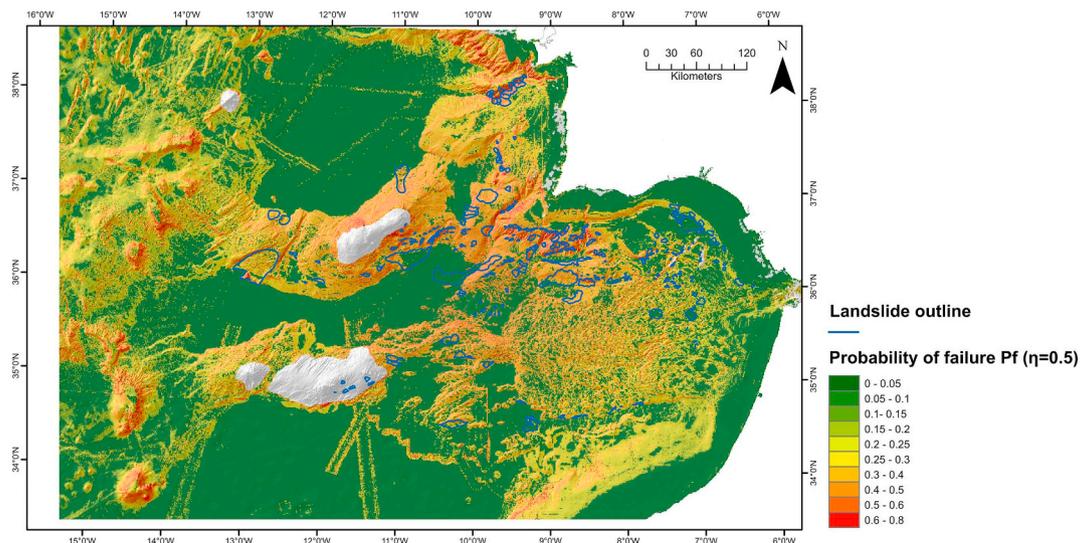
$$(13)$$

Fig. 16. Probability of failure map obtained using a naïve quasi-static slope stability model ($\eta = 0.5$).

Table 5
Summarized statistics of normalized geotechnical parameters after a Bayesian procedure.

	γ/γ'		C_u/σ'_{v_0}	
	$\mu_{\gamma/\gamma'}$	$\sigma_{\mu_{\gamma/\gamma'}}$	$\mu_{C_u/\sigma'_{v_0}}$	$\sigma_{\mu_{C_u/\sigma'_{v_0}}}$
Prior range [max-min]	[5.2–1.95]	[0.4–0.1]	[1.45–0.1]	[0.3–0.01]
Likelihood Estimate	2.28	0.28	0.42	0.25
Updated μ_{XD}	2.26	0.23	0.41	0.16
90% inter-percentile updated	[2.83–1.81]		[0.72–0.19]	
Prior range [max-min]	$\mu_{\sigma_{\gamma/\gamma'}}$ [0.75–0.02]	$\sigma_{\sigma_{\gamma/\gamma'}}$ [0.12–0.02]	$\mu_{\sigma_{C_u/\sigma'_{v_0}}}$ [1.75–0.1]	$\sigma_{\sigma_{C_u/\sigma'_{v_0}}}$ [0.4–0.01]
Likelihood Estimate	0.18	0.1	0.45	0.33
Updated σ_{XD}	0.17	0.06	0.43	0.19
90% inter-percentile updated	[0.32–0.06]		[0.8–0.17]	

with:

$r_u = \frac{\Delta u}{\sigma'_{v0}}$ being the excess pore pressure ratio.

The r_u is a new variable that may be integrated in the spatial model using a similar procedure to that applied here to the slope gradient and *PGA* variables. A local (i.e. grid cell dependent) distribution of overpressure across *SW* the Iberian margin could be derived from spatially distributed inputs such as sedimentation rate and/or sediment accumulation over a reference horizon of known age. Correlations may be established between sedimentation rate and maximum pore water pressure at a cell, by exploiting systematic 1D simulations of sedimentation and consolidation, with a parametric coverage relevant for the SW Iberian margin. Uncertainties in hydromechanical parameters (e.g., permeability and coefficient of consolidation) may be treated using a similar Bayesian approach to that used here for undrained strength or density. Consideration of non-uniform overpressure conditions along the sedimentary sequence would be more realistic, but will require a substantial modification of the stability model, implying at least local vertical discretization (as done, for instance, in Strasser et al., 2011). This extra dimension per grid cell will would add substantial computational and data acquisition costs.

Similar considerations would apply if a variable overconsolidation profile with depth is introduced. Overconsolidation could be considered if the amount of erosion can be estimated and characterized by the corresponding normalized strength ratios at each cell. Alternatively, it could be possible to use non-linear strength profiles at each cell, but that would typically require some numerical solution by limit equilibrium or other method. This latter solution would strongly increase the computational cost of the model. Both would also likely require better geotechnical information than what is currently available.

6.4. From submarine landslide susceptibility to submarine landslide hazard

As noted in the introduction susceptibility maps onshore are frequently conceived as steps towards hazard evaluation. Landslide generated tsunami is the more relevant hazard at the regional scale discussed here.

From a general viewpoint, landslide hazard (H_L) can be expressed as the conditional probability of landslide size (P_{LV}), of landslide occurrence in an established period (P_N) and of landslide spatial occurrence (S) (Guzzetti et al., 2005). Assuming independence amongst the three probabilities, the landslide hazard can therefore be expressed as:

$$H_L = P_{LV} \times P_N \times S \qquad (14)$$

For earthquake triggering the occurrence of landslides is directly connected to the recurrence of seismic shaking. Gutenberg-Richter laws have been proposed for several zones offshore Portugal for seismic hazard studies in that country (Costa et al., 2008). These laws may be easily coupled to the model to provide a starting point to evaluate submarine landslide recurrence until better studies become available. A more complex issue is that of landslide size. Regional magnitude-frequency relations for submarines landslides (Urgeles and Camerlenghi, 2013) might be useful to constraint the parameters affecting the predicted hazard. It is also attractive to explore if the spatial coherence of model outputs (i.e. the connectivity of failed cells for source events of similar magnitude at given location) may be exploited to define an aerial event size. Areal sizes thus estimated would require transformation into volumetric landslide characteristics making use of regional correlations. Considering the spatial correlation structure of outputs might, however, require more detailed consideration of spatial correlations of geotechnical inputs. This can be facilitated by using a random field approach (Fenton and Griffiths, 2008), which is already implemented in the code.

7. Conclusion

This study, using the *SW* Iberian margin as an example, is the first attempt to assess in a systematic probabilistic manner earthquake-induced submarine landslide susceptibility for a large offshore region. A grid cell-based methodology using infinite slope models is applied at this regional-scale. While similar mapping efforts have been previously presented, the area addressed here is orders of magnitude larger than that of the precedents.

The expected seismic shaking across the study area is computed assuming that faults dislocate their entire length, a constrain given by the source database. Therefore, the seismic scenario considered is defined by severe magnitude earthquakes implying long return periods. Given the temporal scale of the landslide catalogue used for validation of the method this appears as a valid assumption.

Despite the jump in scale introduced, well-established evaluation methods for susceptibility maps suggest that the models employed achieve good accuracy. It appears that most landslides included in the database employed to validate the output were earthquake-triggered by the faults collected in the source database. Naturally, this conclusion should be revised and confirmed as both databases are enlarged and/or improved.

The methodology employed has been deliberately developed to facilitate reevaluation, as the database of mapped landslides, the seismic source catalogue or the regional geotechnical information is extended and updated. The method can be also extended to include additional contributing factors such as overpressure. Probabilistic susceptibility maps like the ones presented here are one significant step towards landslide -generated tsunami hazard estimation at the regional scale. However, further work is still necessary to that end, particularly in order to link spatial susceptibility and overall event magnitude.

Notation

The following symbols are used in this paper:

$\sigma_{\varepsilon_{DEM}}$ standard deviation of DEM error

$\mu_{\log(PGA)}$ mean value of logarithm of PGA

Table 6
Percent of landslide-grid-cells predicted by the models.

Optimal thresholds	% landslide grid-cell predicted Pseudo-static approach	% landslide grid-cell predicted Displacement-based approach
$P_f = 0.22$	92%	–
$P_{exceedance\ [Dn=5.2cm]} = 0.135$	–	82%

$\sigma_{\log(PGA)}$	standard deviation of logarithm of PGA
μ_{PGA}	mean value of PGA
σ_{PGA}	standard deviation of PGA
X	statistics of interest (mean and standard deviation) modeled as random variable
$f_X'(x)$	*Prior* probability density function for X
$f_X''(x)$	*Posterior* probability density function for X
$L(x)$	*Likelihood* or conditional probability of observing the Data when $X = x$,
μ_X	logarithm of a possible mean for the variable X
σ_X	logarithm of a possible standard deviation value for the variable X
ξ_i	i-th data on geotechnical statistics
ξ	data vector on geotechnical statistics
σ_{ξ_0}	original standard deviation of ξ
ε_T	transformation error due to regression used
σ_{ε_T}	standard deviation of data statistics ξ due to transformation error used
σ_{x_0}	original standard deviation of the *Likelihood L(x)*
$\sigma_{\varepsilon_{T,W}}$	weighted standard deviation of data statistics ξ due to transformation error used
ε_{μ_T}	transformation error of the predicted mean value
$\mu_{\varepsilon_{\mu T}}$	mean value of $\varepsilon_{\mu T}$
$\sigma_{\varepsilon_{\mu T}}$	standard deviation of $\varepsilon_{\mu T}$
$\mu_{Cu_{vane}}$	mean value of undrained vane shear strength
$\mu_{Cu_{fall-cone}}$	mean value of undrained fall-cone strength
N_s	number of regional sites considered in the updating operation
N_{tot}	number of relevant data
N_T	number of data affected also by the transformation error

Declaration of Competing Interest

The authors declare that they have no known competing financial interests or personal relationships that could have appeared to influence the work reported in this paper.

Acknowledgment

References

Ambraseys, N.N., Douglas, J., Sarma, S.K., 2005. Equations for the estimation of strong ground motions from shallow crustal earthquakes using data from Europe and the Middle East: horizontal peak ground acceleration and spectral acceleration. Bull. Earthq. Eng. 3 (1), 1–53. https://doi.org/10.1007/s10518-005-0183-0.

Baecher, G.B., Christian, J.T., 2005. Reliability and Statistics in Geotechnical Engineering. John Wiley & Sons.

Baptista, M.A., Miranda, J.M., 2009. Revision of the Portuguese catalog of tsunamis. Nat. Hazards Earth Syst. Sci. 9, 25–42. https://doi.org/10.5194/nhess-9-25-2009.

Baptista, M.A., Heitor, S., Miranda, J.M., Miranda, P., Victor, L.M., 1998. The 1755 Lisbon tsunami; evaluation of the tsunami parameters. J. Geodyn. 25, 143–157. https://doi.org/10.1016/S0264-3707(97)00019-7.

Baraza, J., Ercilla, G., Nelson, H., C., 1999. Potential geologic hazards on the eastern Gulf of Cadiz slope (SW Spain). Mar. Geol. 155 (1–2), 191–215.

Bartolome, R., Gracia, E., Stich, D., Martinez-Loriente, S., Klaeschen, D., de Lis Mancilla, F., Lo Iacono, C., Danobeitia, J.J., Zitellini, N., 2012. Evidence for active strike-slip faulting along the Eurasia-Africa convergence zone: Implications for seismic hazard in the southwest Iberian margin. Geology 40, 495–498. https://doi.org/10.1130/G33107.1.

Basili, R., Kastelic, V., Demircioglu, M.B., Garcia Moreno, D., Nemser, E.S., Petricca, P., Sboras, S.P., Besana-Ostman, G.M., Cabral, J., Camelbeeck, T., Caputo, R., Danciu, L., Domac, H., Fonseca, J., García-Mayordomo, J., Giardini, D., Glavatovic, B., Gulen, L., Ince, Y., Pavlides, S., Sesetyan, K., Tarabusi, G., Tiberti, M.M., Utkucu, M., Valensise, G., Vanneste, K., Vilanova, S., Wössner, J., 2013. The European Database of Seismogenic Faults (EDSF) Compiled in the Framework of the Project SHARE. https://doi.org/10.6092/ingv.it-share-edsf.

Behrmann, J.H., Völker, D., Geersen, J., Harders, R., Weinrebe, W., 2014. Size-Frequency Relationship of Submarine Landslides at Convergent Plate Margins: Implications for Hazard and Risk Assessment. In: Krastel, S., Behrmann, J.-H., Völker, D., Stipp, M., Berndt, C., Urgeles, R., Chaytor, J., Huhn, K., Strasser, M., Harbitz, C.B. (Eds.), Submarine Mass Movements and their Consequences, advances in Natural and Technological Hazards Research. Springer International Publishing, pp. 165–175.

Bisch, P., Charvalho, E., Deege, H., Fajir, P., Fardis, P., Franchin, P., Kreshlin, M., Pecker, A., Pinto, P., Plumier, A., Somoja, H., Tsionis, G., 2012. Eurocode 8: SeismicDesign of Buildings Worked examples. Luxemburg. Publications Office of the European Union.

Bommer, J.J., Stafford, P.J., Alarcón, J.E., Akka, S., 2007. The Influence of Magnitude Range on Empirical Ground-Motion Prediction. Bull. Seismol. Soc. Am. 97 (6), 2152–2170.

Borrell, N., Somoza, L., León, R., Medialdea, T., Gonzalez, F.J., Gimenez-Moreno, C.J., 2016. GIS Catalogue of Submarine Landslides in the Spanish Continental Shelf: Potential and Difficulties for Susceptibility Assessment. In Submarine Mass Movements and their Consequences. Springer, Cham, pp. 499–508.

Bray, J.D., Rathje, E.M., 1998. Earthquake-induced displacements of solid-waste landfills. J. Geotech. Geoenviron. 124 (3), 242–253.

Buforn, E., Sanz de Galdeano, C., Udías, A., 1995. Seismotectonics of the Ibero-Maghrebian region. Tectonophysics, Focal Mechanism and Seismotectonics 248, 247–261. https://doi.org/10.1016/0040-1951(94)00276-F.

Buforn, E., Bezzeghoud, M., Udías, A., Pro, C., 2004. Seismic Sources on the Iberia-African Plate Boundary and their Tectonic Implications. Pure Appl. Geophys. 161 https://doi.org/10.1007/s00024-003-2466-1. 623–646.

Cantarino, I., Carrion, M.A., Goerlich, F., Ibañez, V.M., 2019. A ROC analysis-based classification method for landslide susceptibility maps. Landslides 16 (2), 265–282.

Carlton, B.D., Price, K., Vanneste, M., Forsberg, C.F., 2017. Development and application of a regional slope stability assessment screening tool. In Landslides in Sensitive Clays. Springer, Cham.: 267-276.

Chauhan, S., Sharma, M., Arora, M.K., 2010. Landslide susceptibility zonation of the Chamoli region, Garhwal Himalayas, using logistic regression model Landslides 7. pp. 411–423. https://doi.org/10.1007/s10346-010-0202-3.

Chaytor, J.D., ten Brink, U.S., Solow, A.R., Andrews, B.D., 2009. Size distribution of submarine landslides along the U.S. Atlantic margin. Mar. Geol. 264, 16–27. https://doi.org/10.1016/j.margeo.2008.08.007.

Ching, J., Phoon, K.K., 2014. Transformations and correlations among some clay parameters — the global database. Can. Geotech. J. 51 (6), 663–685.

Corominas, J., van Westen, C., Frattini, P., Cascini, L., Malet, J.-P., Fotopoulou, S., Catani, F., Van Den Eeckhaut, M., Mavrouli, O., Agliardi, F., Pitilakis, K., Winter, M.G., Pastor, M., Ferlisi, S., Tofani, V., Hervás, J.T., 2014. Recommendations for the quantitative analysis of landslide. Risk Bull. Eng. Geol 73 (2), 209–263.

Costa, A.C., Sousa, M.L., Carvalho, A., 2008. Seismic zonation for Portuguese national annex of Eurocode 8. Proc. 14WCEE (Beijing, China, October 12-17).

Dreyfus, D., Rathje, E.M., Jibson, R.W., 2013. The Influence of Different Simplified Sliding-Block Models and Input Parameters on Regional Predictions of Seismic Landslides Triggered by the Northridge Earthquake: Engineering Geology, 163, 41–54. https://doi.org/10.1016/j.enggeo.2013.05.015.

De Blasio, F.V., Engvik, L., Harbitz, C.B., Elverhøi, A., 2004. Hydroplaning and submarine debris flows. J. Geophys. Res. 109. https://doi.org/10.1029/2002JC001714.

EMODnet Bathymetry Consortium, 2018. EMODnet Digital Bathymetry (DTM). https://doi.org/10.12770/18ff0d48-b203-4a65-94a9-5fd8b0ec35f6.

Elverhøi, A., Harbitz, C.B., Dimakis, P., Mohrig, D., Marr, J., Parker, G., 2000. On the dynamics of subaqueous debris flows. Oceanography 13 (3), 109–117.

Fenton, G.A., Griffiths, D.V., 2008. Risk Assessment in Geotechnical Engineering. vol. 461 John Wiley & Sons, New York.

Frattini, P., Crosta, G., Carrara, A., 2010. Techniques for evaluating the performance of landslide susceptibility models. Eng. Geol. 11, 62–72.

Fukao, Y., 1973. Thrust faulting at a lithospheric plate boundary the Portugal earthquake of 1969. Earth Planet. Sci. Lett. 18, 205–216. https://doi.org/10.1016/0012-821X(73)90058-7.

Geist, E.L., 2000. Origin of the 17 July 1998 Papua New Guinea Tsunami: earthquake or Landslide. Seismol. Res. Lett. 71, 344–351. https://doi.org/10.1785/gssrl.71.3.344.

Goetz, J.N., Brenning, A., Petschko, H., Leopold, P., 2015. Evaluating machine learning and statistical prediction techniques for landslide susceptibility modeling. Comput. Geosci. 81, 1–11.

Gràcia, E., Lo Iacono, C., 2008. Review of tsunami sources due to slope instabilities in the Gulf of Cadiz. NEAREST project Deliverable D2. Task 1.2: leader CSIC.

Gràcia, E., Dañobeitia, J., Verges, J., the Parsifal Team, 2003. Mapping active faults offshore Portugal (36_N–38_N): implications for the seismic hazard assessment along the southwest Iberian margin. Geology 31, 83–86.

Grezio, A., Babeyko, A., Baptista, M.A., Behrens, J., Costa, A., Davies, G., Geist, E.L., Glimsdal, S., González, F.I., Griffin, J., Harbitz, C.B., 2017. Probabilistic tsunami hazard analysis: multiple sources and global applications. Rev. Geophys. 55 (4), 1158–1198.

Grilli, S.T., Taylor, O.D.S., Baxter, C.D., Maretzki, S., 2009. A probabilistic approach for determining submarine landslide tsunami hazard along the upper east coast of the United States. Mar. Geol. 264 (1–2), 74–97.

Guzzetti, F., Reichenbach, P., Cardinali, M., Galli, M., Ardizzone, F., 2005. Probabilistic landslide hazard assessment at the basin scale. Geomorphology 72, 272–299. https://doi.org/10.1016/j.geomorph.2005.06.002.

Guzzetti, F., Reichenbach, P., Ardizzone, F., Cardinali, M., Galli, M., 2006. Estimating the quality of landslide susceptibility models. Geomorphology 81, 166–184. https://doi.org/10.1016/j.geomorph.2006.04.007.

Hanquiez, V., Mulder, T., Lecroart, P., Gonthier, E., Marchès, E., Voisset, M., 2007. High resolution seafloor images in the Gulf of Cadiz, Iberian margin. Mar. Geol. 246, 42–59.

Hayes, D.E., Pimm, A.C., et al., 1972. Initial Reports of the Deep Sea Drilling Project, 14, Initial Reports of the Deep Sea Drilling. Government Printing Office, Project. U.S. https://doi.org/10.2973/dsdp.proc.14.1972.

Hinz, K., Winterer, E.L., Baumgartner, P.O., Bradshaw, M.J., Channell, J.E.T., Jaffrezo, M., Jansa, L.F., Leckie, R.M., Moore, J.N., Rullkötter, J., Schaftenaar, C., Steiger, T.H., Vuchev, V., Wiegand, G.E., 1984. Initial Reports of the Deep Sea Drilling Project, 79, Initial Reports of the Deep Sea Drilling. Government Printing Office, Project. U.S. https://doi.org/10.2973/dsdp.proc.79.1984.

Hitchcock, C., Givler, R., Angell, M., Hooper, J., 2010. GIS-Based Assessment of Submarine Mudflow Hazard Offshore of the Mississippi Delta, Gulf of Mexico. In: Mosher, D.C., Shipp, R.C., Moscardelli, L., Chaytor, J.D., Baxter, C.D.P., Lee, H.J., Urgeles, R. (Eds.), Submarine Mass Movements and their Consequences, Advances in Natural and Technological Hazards Research. Springer Netherlands. pp. 353–364.

Hensen, C., et al., 2015. Strike-slip faults mediate the rise of crustal-derived fluids and mud volcanism in the deep sea. Geology 43 (4), 339–342. https://doi.org/10.1130/G36359.1.

Huhn, K., Arroyo, M., Cattaneo, A., Clare, M.A., Gràcia, E., Harbitz, C.B., Sebastian Krastel, S., Kopf, A., Finn Løvholt, F., Rovere, M., Strasser, M., Talling, P.J., Urgeles, R., 2019. Modern Submarine Landslide Complexes: a Short Review. Submarine Landslides: Subaqueous Mass Transport Deposits from Outcrops to Seismic Profiles, Geophysical Monograph 246. pp. 183–200.

Hühnerbach, V., Masson, D.G., partners of the COSTA project, 2004. Landslides in the North Atlantic and its adjacent seas: An analysis of their morphology, setting and behavior. Mar. Geol. 213, 343–362. https://doi.org/10.1016/j.margeo.2004.10.013.

Jibson, R.W., 2007. Regression models for estimating coseismic landslide displacement. Eng. Geol. 91, 209–218.

Jibson, R.W., 2011. Methods for assessing the stability of slopes during earthquakes—a retrospective. Eng. Geol. 122 (1–2), 43–50.

Jibson, R.W., Harp, E.L., Jhon, A.M., 2000. A method for producing digital probabilistic seismic landslide hazard maps. Eng. Geol. 58, 271–289. https://doi.org/10.1016/S0013-7952(00)00039-9.

Lee, H., Baraza, J., 1999. Geotechnical characteristics and slope stability in the Gulf of Cadiz. Mar. Geol. 155, 173–190.

Lee, H., Edwards, B.D., 1986. Regional method to assess offshore Slope stability. J. Geotech. Eng. 112 (5), 489–509.

Lee, H., Locat, J., Dartnell, P., Israel, K., Wong, F., 1999. Regional variability of slope stability: application to the Eel margin, California. Mar. Geol. 154 (1–4), 305–321.

Leon, R., Somoza, L., 2011. GIS-based mapping for marine geohazards in seabed fluid leakage areas (Gulf of Cadiz, Spain). Mar. Geophys. Res. 32, 207–223.

Llopart, J., Urgeles, R., Camerlenghi, A., Lucchi, R.G., Rebesco, M., De Mol, B., 2015. Late Quaternary development of the Storfjorden and Kveithola Trough Mouth fans, northwestern Barents Sea. Quat. Sci. Rev. 129, 68–84. https://doi.org/10.1016/j.quascirev.2015.10.002.

Lo Iacono, C., Gràcia, E., Zaniboni, F., Pagnoni, G., Tinti, S., Bartolomé, R., Masson, D.G., Wynn, R.B., Lourenço, N., de Abreu, M.P., Dañobeitia, J.J., Zitellini, N., 2012. Large, deepwater slope failures: implications for landslide-generated tsunamis. Geology 40, 931–934. https://doi.org/10.1130/G33446.1.

Løvholt, F., Schulten, I., Mosher, D., Harbitz, C., Krastel, S., 2019. Modelling the 1929 Grand 551 banks slump and landslide tsunami. In: In Subaqueous Mass Movements, Volume 477 of Special Publications. The Geological Society of London.

Lu, T., Bryant, W.R., 1997. Comparison of Vane Shear and Fall Cone Strengths of Soft Marine Clay. Mar. Georesour. Geotechnol. 15, 67–82.

Mackenzie, B., Hooper, J., Rushton, D., 2010. Spatial Analysis of Shallow Slope Instability Incorporating an Engineering Geological Ground Model. In: Mosher, D.C., Shipp, R.C., Moscardelli, L., Chaytor, J.D., Baxter, C.D.P., Lee, H.J., Urgeles, R. (Eds.), Submarine Mass Movements and their Consequences. Springer Netherlands, Dordrecht, pp. 365–376. https://doi.org/10.1007/978-90-481-3071-9_30.

Martínez-Loriente, S., Sallarès, V., Gràcia, E., Bartolome, R., Dañobeitia, J.J., Zitellini, N., 2014. Seismic and gravity constraints on the nature of the basement in the Africa-Eurasia plate boundary: New insights for the geodynamic evolution of the SW Iberian margin. J. Geophys. Res. Solid Earth 119, 127–149. 10.1002/2013JB010476.

Mayne, P., 2014. Interpretation of geoparameters from seismic piezocone tests (Keynote at CPT'14, Las Vegas). Conference: 3rd International Symposium on Cone Penetration Testing Proceedings. Las Vegas, Nevada. https://doi.org/10.13140/2.1.1694.3680.

Mesri, G., Huvaj, N., 2007. Shear strength mobilized in undrained failure of soft clay and silt deposits. In Advances in Measurement and Modeling of Soil Behavior (pp. 1-22).

Mezcua, J., García Blanco, R.M., Rueda, J., 2008. On the strong ground motion attenuation in Spain. Bull Seism Soc Am 98, 1342–1353.

Minning, M., Hebbeln, D., Hensen, C., Kopf, A., 2006. Geotechnical and geochemical investigations of the Marqués de Pombal landslide at the Portuguese continental margin. Nor. J. Geol. 86, 187–198.

Morgenstern, N.R., 1967. Submarine slumping and the initiation of turbidity currents. In: Richards, A. (Ed.), Marine Geotechnique. Univ. of Ill. Press, Urbana, pp. 189–210.

Mudron, I., Podhoranyi, M., Cirbus, J., Devečka, B., Bakay, L., 2013. Modelling the Uncertainty of Slope Estimation from a Lidar-Derived Dem: a Case Study from a Large-Scale Area in the Czech Republic. GeoSci. Eng. 5, 25–39.

Mulder, T., Gonthier, E., Lecroart, P., Hanquiez, V., Marches, E., Voisset, M., 2009. Sediment failures and flows in the Gulf of Cadiz (eastern Atlantic). Mar. Pet. Geol. 26, 660–672.

Newmark, N.M., 1965. Effects of earthquakes on dams and embankments. Geotechnique 15, 139–160.

Pajarón, L., Fernandez-Puga, M.C., Vazquez, J.T., Lopez-Baeza, E., Fernandez-Salas, L.M., 2015. Caracterización de deslizamientos submarinos en el sector nororiental del talud superior y medio del Golfo de Cádiz (SO de la Península Ibérica), in: Resúmenes Sobre El VIII Simposio MIA15: 173–176.

Pampell-Manis, A., Horrillo, J., Shigihara, Y., Parambath, L., 2016. Probabilistic assessment of landslide tsunami hazard for the northern Gulf of Mexico. J. Geophys. Res. Oceans 121 (1), 1009–1027. https://doi.org/10.1002/2015JC011261.

Park, H.J., Lee, J.H., Woo, I., 2013. Assessment of rainfall-induced shallow landslide susceptibility using a GIS-based probabilistic approach. Eng. Geol. 161, 1–15.

Phoon, K.K., Kulhawy, F.H., 1999a. Characterization of geotechnical variability. Can. Geotech. J. 36 (4), 612–624.

Piedade, A., Alves, T.M., Zêzere, J.L., 2018. A new approach to assess ancient marine slope instability using a bivariate statistical method. Mar. Geol. 401, 129–144.

Piper, D.J.W., Cochonat, P., Morrison, M.L., 1999. The sequence of events around the epicentre of the 1929 Grand Banks earthquake: initiation of debris flows and turbidity current inferred from sidescan sonar. Sedimentology 46, 79–97. https://doi.org/10.1046/j.1365-3091.1999.00204.x.

Puzrin, A.M., Rushton, D., Mackenzie, B., Germanovich, L.N., Randolph, M., 2017. Submarine landslides-stability analysis and risk assessment for offshore developments. In: Carlton, J., Jukes, P., Choo, Y.S. (Eds.), Encyclopedia of Maritime and Offshore Engineering. John Wiley & Sons, Ltd, Chichester, UK, pp. 1–13. https://doi.org/10.1002/9781118476406.emoe521.

Rampello, S., Callisto, L., Fargnoli, P., 2010. Evaluation of Slope Performance under Earthquake Loading Conditions. Rivista Italiana Di Geotecnica 4, 30–41.

Reichenbach, P., Rossi, M., Malamud, B.D., Mihir, M., Guzzetti, F., 2018. A review of statistically-based landslide susceptibility models. Earth Sci. Rev. 180, 60–91. https://doi.org/10.1016/j.earscirev.2018.03.001.

Rodriguez-Peces, M.J., Perez-Garcia, J.L., Mayordomo, J.G., Azañon, J.M., Insua-Arèvelo, J.M., Delgado-Garcia, J., 2011. Applicability of Newmark method at regional, sub-regional and site scales: seismically induced Bullas and La Paca rock-slide cases (Murcia, SE Spain). Natural Hazrad 59, 1109–1124. https://doi.org/10.1007/s11069-011-9820-x.

Sassa, S., Takagawa, T., 2018. Liquefied gravity flow-induced tsunami: first evidence and comparison from the 2018 Indonesia Sulawesi earthquake and tsunami disasters. Landslides. https://doi.org/10.1007/s10346-018-1114-x.

Scassera, G., Stewart, J.P., Kayen, R.E., Lanzo, G., 2009. Database for Earthquake Strong Motion Studies in Italy Journal of Earthquake Engineering. 13. pp. 852–881. 2009. https://doi.org/10.1080/13632460802566997.

Sousa, M.L., Oliveira, C.S., 1997. Hazard assessment based on macroseismic data considering the influence of geological conditions. Natural Hazards. 14: 207-225, Kluwer Academic Publishers.

Stewart, J.P., Blake, T.F., Hollingsworth, R.A., 2003. A screen analysis procedure for seismic slope stability. Earthquake Spectra 19 (3), 697–712.

Stich, D., de Mancilla, F.L., Morales, J., 2005. Crust-mantle coupling in the Gulf of Cadiz (SW-Iberia). Geophys. Res. Lett. 32, L13306. https://doi.org/10.1029/2005GL023098.

Stich, D., de Mancilla, F.L., Pondrelli, S., Morales, J., 2007. Source analysis of the February 12th 2007, Mw 6.0 Horseshoe earthquake: Implications for the 1755 Lisbon earthquake. Geophys. Res. Lett. 34, L12308. https://doi.org/10.1029/2007GL030012.

Stich, D., Martín, R., Morales, J., 2010. Moment tensor inversion for Iberia–Maghreb earthquakes 2005–2008. Tectonophysics 483, 390–398. https://doi.org/10.1016/j.tecto.2009.11.006.

Strasser, M., Hilbe, M., Anselmetti, F.S., 2011. Mapping basin-wide subaquatic slope failure susceptibility as a tool to assess regional seismic and tsunami hazards. Mar. Geophys. Res. 32 (1–2), 331–347.

Straub, D., Papaioannou, I., 2015. Bayesian analysis for learning and updating geotechnical parameters and models with measurements. Risk and reliability in geotechnical engineering 221–264.

Synolakis, C.E., Bardet, J.-P., Borrero, J.C., Davies, H.L., Okal, E.A., Silver, E.A., Sweet, S., 583 Tappin, D. R, 2002. The slump origin of the 1998 Papua New Guinea tsunami. Proceedings of the 584 Royal Society of London. Series A: Mathematical, Physical and Engineering Sciences, 458(2020):763–585 789.

ten Brink, S., Lee, H.J., Geist, E.L., Twichell, D., 2009. Assessment of tsunami hazard to the U.S. East Coast using relationships between submarine landslides and earthquakes. Mar. Geol. 122, 34–42.

Terrinha, P., Matias, L., Vicente, J., Duarte, J., Luís, J., Pinheiro, L., Lourenço, N., Diez, S., Rosas, F., Magalhães, V., Valadares, V., Zitellini, N., Roque, C., Víctor, L.M., 2009. Morphotectonics and strain partitioning at the Iberia–Africa plate boundary from multibeam and seismic reflection data. Mar. Geol. 267, 156–174. https://doi.org/10.1016/j.margeo.2009.09.012.

Urgeles, R., Camerlenghi, A., 2013. Submarine landslides of the Mediterranean Sea: Trigger mechanisms, dynamics, and frequency-magnitude distribution. J. Geophys. Res.: Earth 118, 2600–2618.

Urgeles, R., Locat, J., Lee, H.J., Martin, F., 2002. The Saguenay Fjord, Quebec, Canada: integrating marine geotechnical and geophysical data for spatial seismic slope stability and hazard assessment. Mar. Geol. 185, 319–340.

Urgeles, R., Leynaud, D., Lastras, G., Canals, M., Mienert, J., 2006. Back-analysis and failure mechanisms of a large submarine slide on the ebro slope, NW Mediterranean. Mar. Geol. 226, 185–206. https://doi.org/10.1016/j.margeo.2005.10.004.

Vizcaino, A., Gràcia, E., Pallàs, R., Garcia-Orellana, J., Escutia, C., Casas, D., Willmott, V., Diez, S., Asioli, A., Dañobeitia, J.J., 2006. Sedimentology, physical properties and age of mass transport deposits associated with the Marques de Pombal Fault. Southwest Portuguese Margin.

van Westen, C.J., Castellanos, E., Kuriakose, S.L., 2008. Spatial data for landslide susceptibility, hazard, and vulnerability assessment: an overview. Engineering Geology, Landslide Susceptibility, Hazard and Risk Zoning for Land Use Planning 102, 112–131. https://doi.org/10.1016/j.enggeo.2008.03.010.

Wang, Y., Cao, Z., 2013. Probabilistic characterization of Young's modulus of soil using equivalent samples. Eng. Geol. 159, 106–118.

Wang, Y., Cao, Z., Au, S., K., 2011. Practical reliability analysis of slope stability by

advanced Monte Carlo simulations in a spreadsheet. Can. Geotech. J. 48, 162–172.

Wang, Y., Cao, Z., Li, D., 2016. Bayesian perspective on geotechnical variability and site characterization. Eng. Geol. 203, 117–125.

Zhang, L., Tang, W.H.H., Zhang, L., Zheng, J., 2004. Reducing uncertainty of prediction from Empirical. J. Geotech. Geoenviron. Eng. 130 (5), 526–534.

Zhu, L., Huang, J.-F., 2006. GIS-based logistic regression method for landslide susceptibility mapping in regional scale. J. Zhejiang Univ. Sci. A 7 (12), 2007–2017.

Zitellini, N., Rovere, M., Terrinha, P., Chierici, F., Matias, L., Team, Bigsets, 2004. Neogene through quaternary tectonic reactivation of SW Iberian passive margin. Pure Appl. Geophys. 161, 565–587.

Zitellini, N., Gràcia, E., Matias, L., Terrinha, P., Abreu, M.A., DeAlteriis, G., Henriet, J.P., Dañobeitia, J.J., Masson, D.G., Mulder, T., Ramella, R., Somoza, L., Diez, S., 2009. The quest for the Africa–Eurasia plate boundary west of the Strait of Gibraltar. Earth Planet. Sci. Lett. 280, 13–50. https://doi.org/10.1016/j.epsl.2008.12.005.